A comparative investigation on the microstructure and mechanical properties of additively manufactured aluminum alloys

Muztahid Muhammad [a,b], P.D. Nezhadfar [a,b], Spencer Thompson [c], Ankit Saharan [c], Nam Phan [d], Nima Shamsaei [a,b,*]

[a] Department of Mechanical Engineering, Auburn University, Auburn, AL 36849, USA
[b] National Center for Additive Manufacturing Excellence (NCAME), Auburn University, Auburn, AL 36849, USA
[c] EOS North America, 3813 Helios Way #B298, Pflugerville TX 78660, USA
[d] Structures Division, Naval Air Systems Command (NAVAIR), Patuxent River, MD 20670, USA

ARTICLE INFO

ABSTRACT

Due to exceptional strength/stiffness to weight ratio, aluminum (Al) alloys are being extensively used in many exclusive applications. The microstructure, and consequently, the mechanical properties of additively manufactured (AM) Al alloys are expected to vary compared to those of their conventionally manufactured counterparts due to the unique thermal history experienced during the additive manufacturing (AM) processes. Therefore, it is critical to understand the microstructure and characterize the mechanical properties of AM Al alloys to verify if they meet the requirements for being deployed in the fatigue critical applications. In this study, the microstructure and mechanical properties (i.e., tensile and fatigue) of laser beam powder bed fused (LB-PBF) LPW AlSi10Mg, EOS AlSi10Mg, Scalmalloy, and QuesTek Al alloys are characterized. Room temperature quasi-static tensile tests are conducted at the strain rate of 0.001 s^{-1} on machined surface specimens, and uniaxial fully-reversed strain-controlled fatigue tests are performed on both as-built and machined surface specimens. Some differences in microstructure and tensile properties of the LB-PBF AlSi10Mg fabricated with LPW and EOS powders are noticeable. Among the Al alloys, the LB-PBF Scalmalloy possesses the highest strength and high ductility as well as the highest fatigue resistance credited to its ultrafine/nano-size grains and precipitates. For all the LB-PBF Al alloys investigated, surface micro-notches and volumetric defects (pores, lack of fusion) are found to be the primary sources of fatigue crack initiation in the as-built and machined surface conditions, respectively.

1. Introduction

Aluminum (Al) alloys have been used extensively in various industries such as automotive, aerospace, constructions, and packaging due to their acceptable material properties (e.g., lightweight, high corrosion resistance, high thermal conductivity, excellent machinability, etc.), and economic benefits as compared to steels, and titanium alloys [1,2]. Al alloys are categorized into cast and wrought, based on their microstructure, chemical composition, and process characteristics [2]. Recently, many efforts have been made to manufacture Al alloys via additive manufacturing (AM) technologies due to the benefits provided

(e.g., fabricating lightweight parts with complex geometries) as compared to the conventional manufacturing (CM) methods (e.g., casting, forging, extrusion, etc.) [3,4]. Among different AM techniques, laser beam powder bed fusion (LB-PBF) is one of the most well-developed processes, where the powder is spread on the powder bed, and a high-power density laser is used to melt and fuse metallic powder particles together to fabricate the parts [5].

There are challenges associated with the fabrication of parts using AM techniques; the AM parts experience intricate thermal processing (i.e., rapid melting and solidification), which may affect their microstructure, induce residual stresses, and form process-induced defects such as surface roughness, pores, lack of fusion (LoF), etc. [6,7].

Consequently, the mechanical properties of the AM materials will be impacted; although enhancements in the quasi-static tensile strength of AM materials are often reported as compared to the CM counterparts [8], the fatigue performance of the AM materials are typically compromised by the presence of process-induced defects [9,10]. On top of all the challenges with the AM processes, fabricating Al alloys is even more challenging due to their high thermal conductivity [11] and high reflectivity [12].

Among the various Al alloys, AlSi10Mg is one of the most suitable alloys manufactured via the LB-PBF process owing to its low coefficient of thermal expansion (CTE) [13]. Besides, having a lower CTE as compared to the other Al alloys, AlSi10Mg can be manufactured with better dimensional accuracy and reduced thermal stresses. Several research groups have investigated the high cycle fatigue (HCF) and very high cycle fatigue (VHCF) behavior of LB-PBF AlSi10Mg specimens [14–16]. Jian et al. [15] studied the HCF and VHCF behaviors of LB-PBF AlSi10Mg specimens with different powder particle sizes and without any post-process heat treatments. It was found that specimens fabricated with smaller powder particles had a higher number of defects as compared to those fabricated with larger powder particles. Accordingly, using larger powder particles for manufacture of LB-PBF AlSi10Mg enhanced the fatigue behavior of this material. However, it has been shown that appropriate thermal treatments can positively impact the mechanical properties (i.e., tensile and fatigue) of LB-PBF AlSi10Mg alloy [10,17,18].

There have been several investigations mainly focused on the effect of thermal post-processing (i.e., heat treatment, hot isostatic pressing (HIP)) on the microstructure and mechanical properties of LB-PBF AlSi10Mg [15,17,19,20]. Due to the formation of intercellular Si networks and Mg$_2$Si precipitates during the LB-PBF fabrication [21], the as-fabricated LB-PBF AlSi10Mg has a significantly higher tensile strength and hardness as compared to its CM counterpart after T6 heat treatment. It can be observed from the existing literature that the mechanical properties (i.e., tensile and fatigue) of LB-PBF AlSi10Mg are greatly affected by the thermal treatment [10,18].

Ngnekou et al. [18] studied the effect of heat treatment and build orientation on the tensile and fatigue behavior of LB-PBF AlSi10Mg. They fabricated specimens on the build platform preheated to 200 °C, and post heat treated the specimens following T6 procedure (i.e.,

solutionizing at 540 °C for 8 h/water quenched, followed by aging at 160 °C for 10 h/air cooled). The T6 heat treatment applied in [18] increased the tensile strength of the material by precipitation strengthening mechanism. However, they reported anisotropy in the fatigue performance of T6-treated LB-PBF AlSi10Mg fabricated in different orientations (i.e., vertical vs. horizontal) due to the relative orientation of layers/LoF defects with respect to the loading direction.

On the other hand, Brandl et al. [10] showed that preheating the build platform at higher temperature, 300 °C, along with conducting a different T6 heat treatment procedure (solutionizing at 525 °C for 6 h/ water quenched, followed by aging at 165 °C for 7 h/air cooled) alleviate the build orientation effect on the fatigue performance of LB-PBF AlSi10Mg. They attributed this to the combination of preheating the build platform at a higher temperature (i.e., 300 °C vs. 200 °C in [18]) and a different T6 heat treatment. The latter homogenized the microstructure and removed intercellular Si network, and the former reduced the volumetric defects.

In addition to the AlSi10Mg, other high strength Al alloys have been developed for AM. Scalmalloy, an Sc- and Zr- modified Al alloy, is one of the high-strength Al alloys with excellent weldability introduced to the AM community [22]. In contrast to the typical coarse columnar grain structure reported in most AM materials [23], the LB-PBF Scalmalloy possesses a bimodal microstructure consisting of nano-size equiaxed grains along with fine columnar grains [24]. This is due to the formation of coherent nano-size Al$_3$(Sc,Zr) precipitates during solidification, which pins the grain boundaries and prohibits grain growth [25]. Moreover, heat treating the LB-PBF Scalmalloy has been shown to increase the strength of the material via the precipitation hardening mechanism [26].

Although there are several studies on the microstructural characterization of the LB-PBF Scalmalloy, the evaluation of its mechanical properties is limited to the hardness and tensile properties [27,28]. To the best of the authors' knowledge, there are only a couple of studies available on the fatigue behavior of LB-PBF Scalmalloy [29,30]. Awd et al. [29] investigated the tensile and stress-life fatigue behavior of LB-PBF AlSi10Mg and LB-PBF Scalmalloy in non-heat treated (NHT) condition. The LB-PBF Scalmalloy was found to have superior tensile and fatigue strengths as compared to the LB-PBF AlSi10Mg, owing to its fine microstructure enriched with the Al$_3$Sc precipitates. Begoc et al. [30] developed the process parameters of LB-PBF Scalmalloy and studied the mechanical properties (both tensile and fatigue) in as-built surface condition after conducting heat treatment within 325–350 °C with a duration between 4 and 10 h. They also carried out simulations to examine the applicability of LB-PBF Scalmalloy for thermal applications as well as for the use in radio frequency components. The fatigue results of LB-PBF Scalmalloy in as-built surface condition were compared with sand-blasted LB-PBF AlSi7Mg0.6. The Scalmalloy specimens in as-built surface condition exhibited better fatigue performance compared to the surface treated (i.e., sand-blasted) LB-PBF AlSi7Mg0.6 in the low cycle fatigue (LCF) regime.

According to the AM standardization road map compiled by America Makes & ANSI additive manufacturing standardization collaborative (AMSC) [31], baseline materials data are required to fill the Gap FMP1 on "materials properties" introduced with a high priority. Therefore, this study aims to generate tensile and fatigue data for four different LB-PBF Al alloys: LPW AlSi10Mg, EOS AlSi10Mg, Scalmalloy, and a newly developed Al alloy provided by QuesTek Innovations LLC., at their optimum heat treatment conditions proposed for each alloy in the literature. The fatigue behavior for these alloys is evaluated in the as-built and machined surface conditions. Moreover, the tensile and fatigue behaviors observed will be explained with respect to their microstructure after post heat treatment.

This article is organized as follows: in Section 2, the experimental design of the study is presented in detail. In Section 3, the experimental results, including the microstructure analysis, surface roughness measurements, and mechanical properties (i.e., tensile and fatigue), are

presented. In Section 4, the tensile and fatigue behavior of the LB-PBF Al alloys are discussed and correlated to their microstructure, surface condition, and volumetric defects. Finally, some conclusions drawn based on the experimental observations in this study are listed in Section 5.

2. Experimental procedures

2.1. Material and specimen fabrication

In this study, four different sets of Al alloys were investigated: (1) LPW AlSi10Mg, (2) EOS AlSi10Mg, (3) Scalmalloy, and (4) an Al alloy provided by QuesTek Innovations LLC., which will be addressed as "QuesTek Al" in this manuscript. The QuesTek Al is introduced as a high strength, highly corrosion-resistant, and low-cost alloy (as it contains no expensive alloying elements). The pre-alloyed gas-atomized powder of each alloy was used to manufacture the specimens via the LB-PBF process. The chemical compositions of LPW AlSi10Mg, EOS AlSi10Mg, Scalmalloy, and QuesTek Al are listed in Table 1.

It is worth noting that there are slight differences in the chemical composition of the AlSi10Mg powder provided by LPW with that of the EOS one. The LPW AlSi10Mg and Scalmalloy powders were provided by LPW Technology (now Carpenter Additive®) [32], while the EOS AlSi10Mg powder was provided by the EOS North America. In addition, the QuesTek Al powder was provided by Connecticut Engineering Associates Corporation (CEAC).

All the specimens were fabricated using EOS M290 LB-PBF system. The process parameters used for the AlSi10Mg (both the LPW and EOS batches) were recommended by EOS, while the process parameters for the Scalmalloy were adopted from [33]. The Scalmalloy process parameters used may not necessarily be the most optimized set, yet the only one found in the literature for EOS M290 system. In addition, the process parameters for QuesTek Al were provided by QuesTek Innovations LLC. The process parameters used to fabricate the specimens in this study are listed in Table 2.

It must be noted that no surface process parameter optimization (i.e., contour) was done for the Scalmalloy and QuesTek Al. Hence, the contour process parameters (power of 280 W, scan speed of 350 mm/s, and thickness of 0.12 mm) of AlSi10Mg recommended by EOS were used for these alloys. The printing layout, shown in Fig. 1(a), was the same for all the alloys. As seen, cylindrical rods with 12 mm and 10 mm diameters, both with 90 mm height were fabricated and further machined to the final geometry of the fatigue and tensile round specimens with uniform gage sections, shown in Fig. 1(b) and (c), respectively. To investigate the effect of surface roughness on the fatigue behavior of these alloys, net-shape fatigue specimens with a uniform gage section were also fabricated with the same final dimensions shown in Fig. 1(b).

Table 1
Nominal chemical compositions, provided by the manufacturers, for the Al powder batches characterized in this study.

Wt.%	LPW AlSi10Mg	EOS AlSi10Mg	Scalmalloy	QuesTek Al
Al	Bal.	Bal.	Bal.	Bal.
Si	9.60	9–11	0.20	2.37
Fe	0.18	<0.55	0.10	0.035
Cu	<0.05	<0.05	–	–
Mn	<0.01	<0.45	0.50	0.35
Mg	0.38	0.2–0.45	4.60	6.79
Ni	<0.01	<0.05	–	–
Zn	<0.01	<0.10	–	–
Pb	<0.01	<0.05	–	–
Sn	<0.01	<0.05	–	–
Ti	<0.01	<0.15	–	–
O	0.08	–	0.04	–
Sc	–	–	0.70	–
Zr	–	–	0.30	–

Table 2
The process parameters used for the fabrication of LB-PBF Al specimens in this study.

Alloy	Laser power (W)	Scanning speed (mm/s)	Hatch spacing (mm)	Layer thickness (mm)
LPW AlSi10Mg	370	1300	0.13	0.03
EOS AlSi10Mg	370	1300	0.13	0.03
Scalmalloy	370	1000	0.10	0.03
QuesTek Al	370	1040	0.17	0.03

2.2. Heat treatment

The most optimum heat treatment procedures for obtaining enhanced mechanical properties for each alloy were selected based on the literature and listed in Table 3. The specimens were heat treated after fabrication prior to being cut from the build platform to remove the residual stresses and adjust the microstructure for obtaining improved mechanical properties. All the heat treatment procedures were conducted using an electric oven furnace under argon atmosphere.

Both the LB-PBF LPW and EOS AlSi10Mg specimens were only stress-relieved [36,37]. Although T6 is a very common heat treatment for the wrought AlSi10Mg, it has been shown to result in mechanical anisotropy and make the LB-PBF material more sensitive to the presence of defects during cyclic deformation [18,38]. There are slight differences in the stress-relieve procedures for the LPW and EOS AlSi10Mg materials; the LB-PBF LPW AlSi10Mg parts were stress-relieved based on the most common procedure used in the literature (i.e., 300 °C for 2 h), while the LB-PBF EOS AlSi10Mg parts were undergone the stress-relieve cycle recommended by EOS North America (i.e., 270 °C for 1.5 h). For the LB-PBF Scalmalloy, a post-process thermal treatment of 325 °C-350 °C with a soaking duration of 4–10 h has been reported to result in higher strength due to the formation of $Al_3(Sc,Zr)$ precipitates [39]. Maximum hardness for the LB-PBF Scalmalloy has been reported to be obtained after heat treating at 325 °C for 4 h [27]; accordingly, this heat treatment was used in the current study. For LB-PBF QuesTek Al parts, a post-process thermal treatment of 185 °C with a soaking duration of 2 h was performed according to the recommendation of QuesTek Innovations LLC.

2.3. Microstructure and surface roughness characterizations

Microstructure characterizations were conducted for all the Al alloys on the longitudinal plane parallel to the build direction. The specimens were cut transversely parallel to the build direction, ground, and polished to a mirror-finished surface. Electron backscatter diffraction (EBSD) analysis and electron channeling contrast imaging (ECCI) were conducted to characterize the microstructure. Moreover, the electron dispersive spectroscopy (EDS) was carried out for the chemical analysis, and the EDS maps were generated for the constituent elements in each alloy. All the microstructure characterizations were conducted using a Zeiss Crossbeam 550 SEM/FIB scanning electron microscope (SEM).

A digital optical microscope, Keyence VHX-6000, was used to measure the surface roughness of the as-built specimens. Surface roughness measurements were obtained from 1.5 mm length profiles in the longitudinal direction on the gage section of the as-built fatigue specimens from all sides. The surface roughness measurements were repeated at least five times from different locations of the gage section.

2.4. Mechanical testing

Quasi-static tensile tests were conducted on the specimens with the machined surface condition using an MTS landmark servo-hydraulic load frame with a load cell of 100 kN. An MTS mechanical
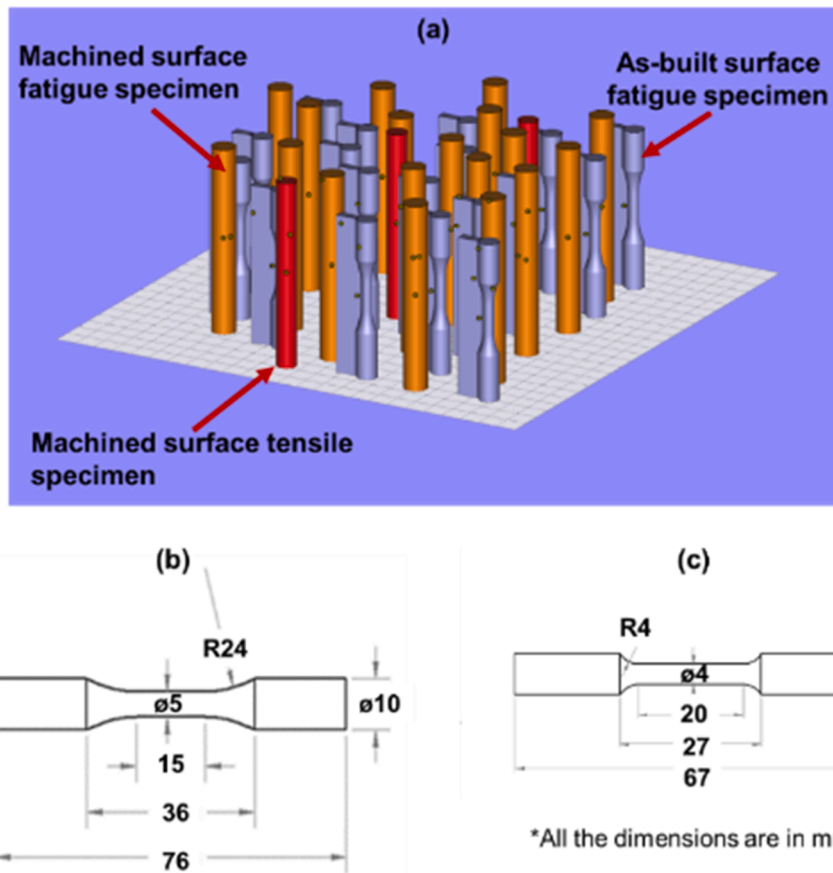
Fig. 1. (a) The print layout, showing different types of specimens fabricated, including fatigue specimens in as-built surface condition, cylindrical rods to be further machined to fatigue and tensile specimens, (b) final geometry of fatigue specimens following the ASTM E606 [34], and (c) final geometry of tensile specimens based on ASTM E08 [35].

Table 3
Heat treatment procedures applied to the LB-PBF Al specimens in this study.

Alloy	Temperature (°C)	Duration (hour)	Quenching environment
LPW AlSi10Mg	300	2	Furnace
EOS AlSi10Mg	270	1.5	
Scalmalloy	325	4	
QuesTek Al	185	2	Air

extensometer was attached to the specimen in the gage section to record the strain during the test. However, due to the limited travel range of the extensometer and to avoid damaging it, the tensile tests were carried out in two steps; the strain-controlled mode up to 0.035 mm/mm strain with an extensometer attached, followed by the removal of the extensometer and displacement-controlled test, up to the fracture of the specimen. The tensile tests were repeated twice for each of the alloys as there were a limited number of specimens available; therefore, one must consider that the results presented herein are only for comparison purposes.

Uniaxial fully-reversed strain-controlled $\left(R_\varepsilon = \frac{\varepsilon_{min}}{\varepsilon_{max}} = -1\right)$ fatigue tests were performed on the Al specimens in both as-built and machined surface conditions following the ASTM E606 testing standard [34]. For the as-built surface specimens, fatigue tests were carried out at strain amplitude levels within the range of 0.00075–0.0030 mm/mm, and for the machined surface specimens, within the range of 0.0010–0.0050 mm/mm. Fatigue tests were conducted until the complete separation of the specimens into two parts (i.e., final fracture), while the specimens exceeding 10^7 reversals were stopped and considered as runout tests. Fractography analysis on the fracture surfaces was further performed on a selected number of fractured specimens, both in as-built and machined

surface conditions, using the SEM to characterize the failure mechanisms for each alloy.

3. Experimental results

In this section, the results of the microstructure characterization, surface roughness analysis, and mechanical properties (i.e., tensile and fatigue) of the LB-PBF Al alloys examined in this study are presented. The differences in the mechanical properties of the LB-PBF Al alloys are correlated to their micro-/defect-structure and discussed with more details in Section 4.

3.1. Microstructure of LB-PBF Al alloys

The inverse pole figure (IPF) maps shown in Fig. 2 represent the microstructure of the heat treated LB-PBF Al alloys on the longitudinal plane parallel to the build direction. It can be seen that the LPW AlSi10Mg (Fig. 2(a)) and EOS AlSi10Mg (Fig. 2(b)) alloys possess more or less similar microstructure constituent of columnar grains. The typical columnar grain structure, in which the grains elongated along the build direction toward the build platform, can be observed for all the LB-PBF Al alloys in Fig. 2. However, the LB-PBF Scalmalloy and LB-PBF QuesTek Al possess finer grain structures (as shown in Fig. 2(c) and (d), respectively), as it can also be noted from the grain size analysis obtained from the EBSD results (following ASTM E2627 standard [40] based on equivalent circle diameter) and presented in Fig. 2(e). The mean grain size for the Scalmalloy, QuesTek Al, LPW AlSi10Mg, and EOS AlSi10Mg is 2.3 μm, 2.6 μm, 5.0 μm, and 5.3 μm, respectively. It is worth mentioning that the average grain size for the LB-PBF Scalmalloy
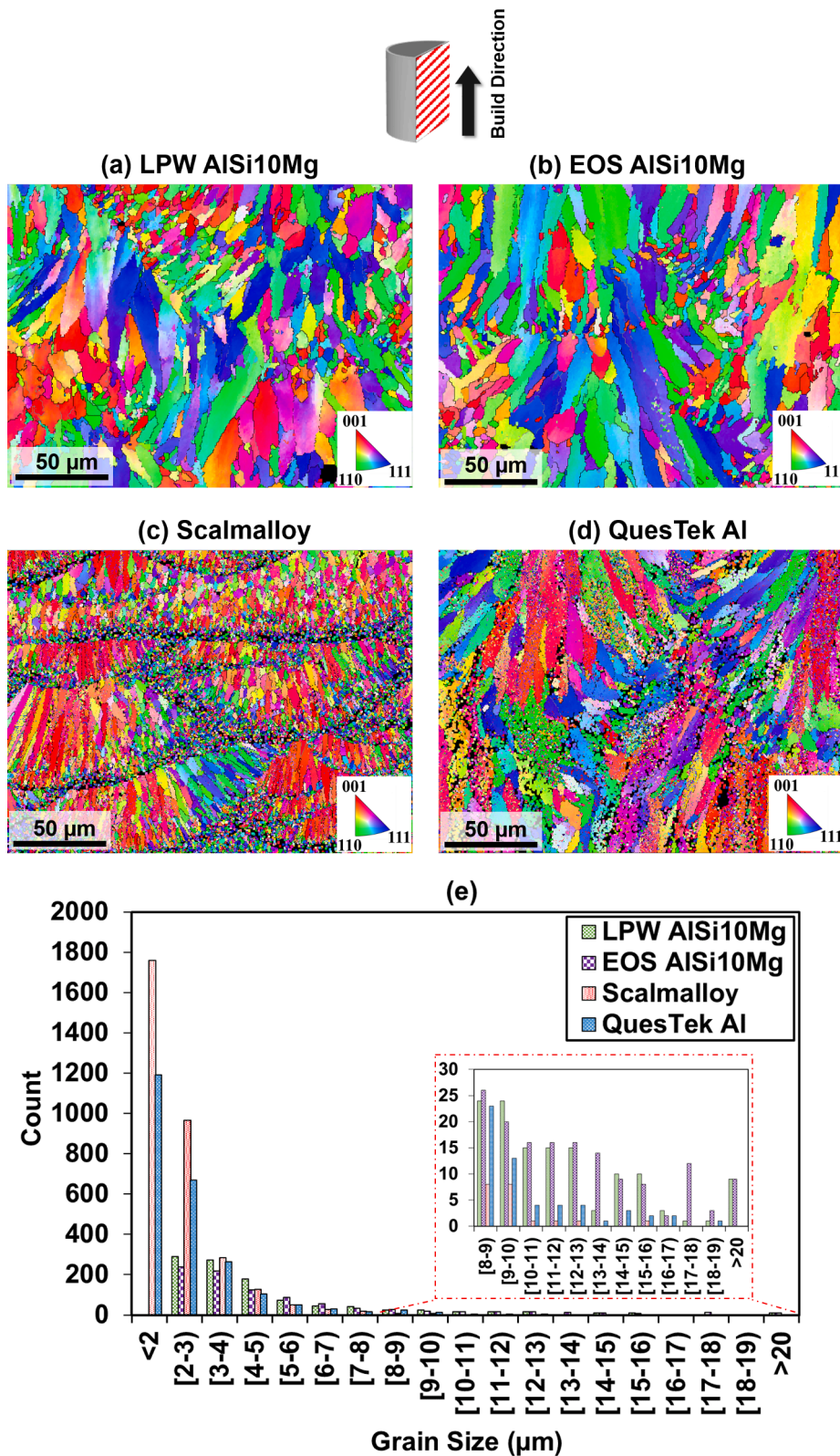
Fig. 2. Microstructure characterization on the longitudinal plane parallel to the build direction; IPF maps for the LB-PBF (a) LPW AlSi10Mg, (b) EOS AlSi10Mg, (c) Scalmalloy, and (d) QuesTek Al. The grain size analysis for these alloys is presented in (e).

may be much lower than 2.3 μm; there are nano-size grains in the melt pool regions which have not been recognized (black regions) with the step size used for the EBSD scans (0.43 μm). Therefore, these small grains may have not been included in the grain size analysis.

The EDS maps and the chemical analysis results for each of the alloys are presented in Fig. 3. It can be seen that the chemical analysis is mostly similar to the nominal chemical composition of the powder batches reported in Table 1, and the alloy elements are homogeneously distributed in the microstructure for all of these LB-PBF Al alloys. The segregation of Si and Mg elements can be seen for the LPW and EOS AlSi10Mg in Fig. 3

(a) LPW AlSi10Mg

Element	Wt%
Al	89.4
Si	9.4
Mg	0.3
Fe	0.2
O	0.7

(b) EOS AlSi10Mg

Element	Wt%
Al	89.6
Si	9.2
Mg	0.3
Fe	0.2
O	0.7

(c) Scalmalloy

Element	Wt%
Al	94.6
Si	0.18
Mg	3.6
Sc	0.7
Zr	0.3
O	0.6

(d) QuesTek Al

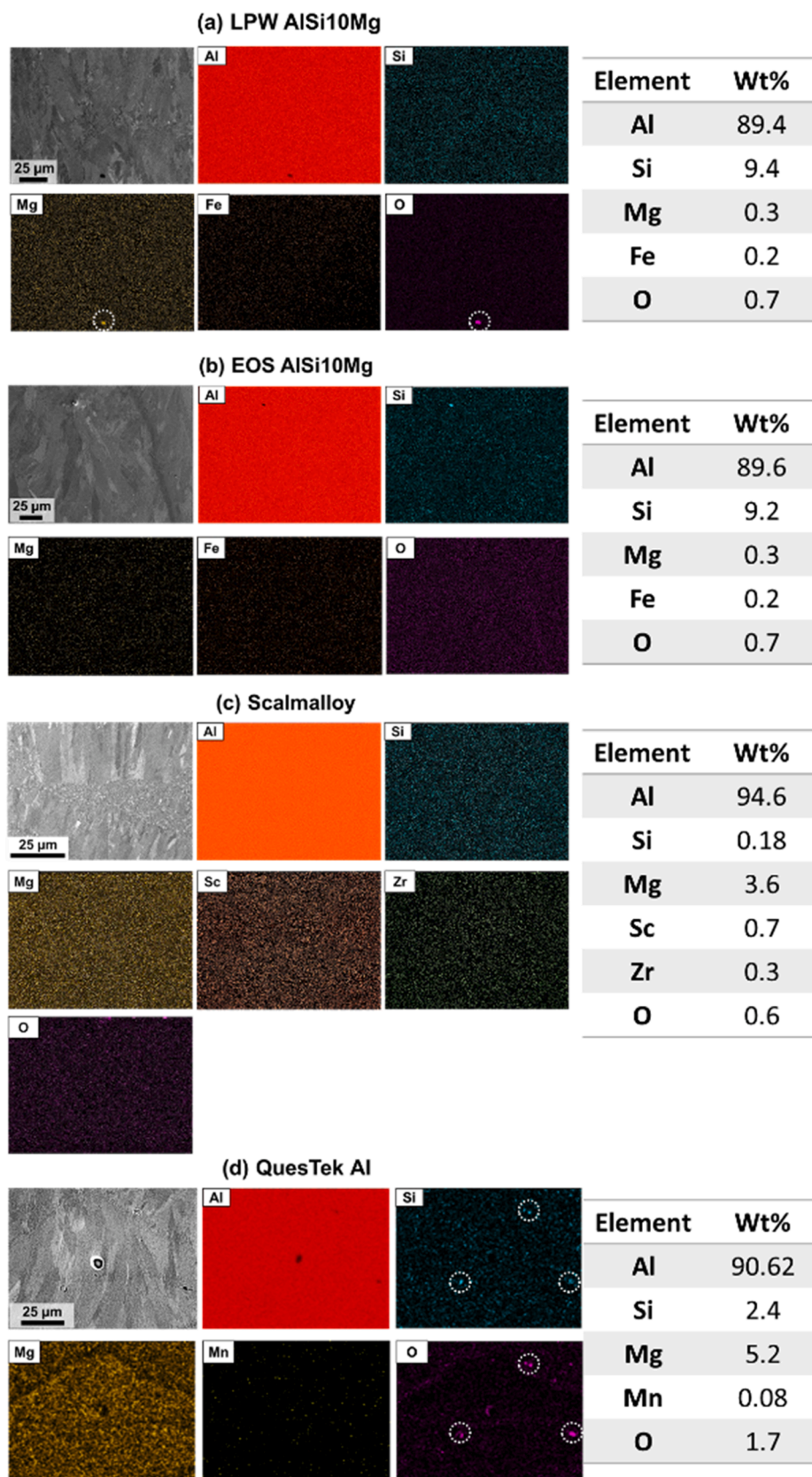| Element	Wt%
Al	90.62
Si	2.4
Mg	5.2
Mn	0.08
O	1.7

Fig. 3. The backscatter diffraction (BSD) images and corresponding EDS maps as well as the chemical analysis results for the LB-PBF (a) LPW AlSi10Mg, (b) EOS AlSi10Mg, (c) Scalmalloy, and (d) QuesTek Al.

(a) and (b), respectively, which can result in the formation of Mg_2Si precipitates in the microstructure. Moreover, it has been reported that, in case there is considerable oxygen (O) content in the material, nano-size (~200–250 nm) Al-Mg oxides enriched with other elements can be formed in the microstructure [20]. It is worth noting as the O is a light element; therefore, the value reported by EDS in Fig. 3 may not be accurate, and it is only reported for comparison purposes. The source of the O content in the material may be either due to the presence of O gas in the chamber or from the oxide layer on the powder particles used for the fabrication [25].

The profoundly refined microstructure of the LB-PBF Scalmalloy (see Fig. 2(c)) is attributed to the formation of coherent nano-size $Al_3(Sc,Zr)$ precipitates during the fabrication [41]. The accumulation and distribution of Sc and Zr elements through the matrix can be seen in Fig. 3(c). These precipitates act as heterogeneous nucleation sites and prohibit grain growth by pinning the grain boundaries, which results in grain refinement. In the case of QuesTek Al alloy (Fig. 3(d)), the O level is much higher than that of the LPW and EOS AlSi10Mg alloys. In addition, as the Si is uniformly distributed in the matrix, the formation of SiO_2 is probable, wherever there is an accumulation of O (the Si and O accumulated at the same location are circled in Fig. 3(d)).

3.2. Surface roughness analysis

A representative surface profile of the specimens with the as-built surface condition and the corresponding standard surface roughness parameters (i.e., arithmetic average surface roughness, R_a, maximum valley depth of the surface roughness profile, R_v, and maximum peak-to-valley height of the profiled line, R_t according to ISO 4287 [42]) for each of the LB-PBF Al alloys are shown in Fig. 4 and Fig. 5, respectively. As seen, both the LB-PBF LPW and EOS AlSi10Mg specimens have a smooth surface as compared to those of the LB-PBF Scalmalloy and LB-PBF QuesTek Al ones. The discrepancy in surface roughness profiles (see Fig. 4) can be attributed to the surface process parameters (i.e., contour) used to fabricate the as-built specimens. The surface process parameters for LB-PBF LPW and EOS AlSi10Mg were optimized; therefore, relatively low surface roughness values with small standard deviations (according to R_a, R_v, and R_t measurements shown in Fig. 5) are obtained. On the other hand, the LB-PBF Scalmalloy and LB-PBF QuesTek Al specimens were fabricated using non-optimized surface process parameters, resulting in much higher surface roughness for these specimens. It is worth mentioning that, QuesTek Al specimens have the highest standard deviation for R_t (see Fig. 5), which is associated with the significantly
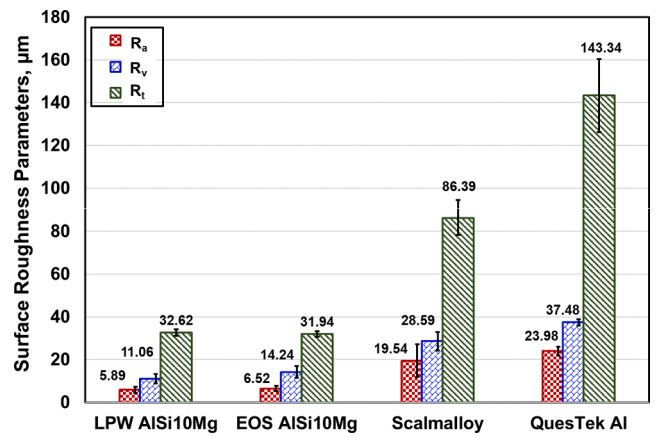

Fig. 5. Arithmetic average surface roughness, R_a, maximum valley depth of the surface roughness profile, R_v, and maximum peak-to-valley height of the profiled line, R_t, of the LB-PBF Al specimens with the as-built surface condition. The higher surface roughness of Scalmalloy and QuesTek Al specimens may be related to the non-optimized surface process parameters used during their fabrication.

large anomalous peaks on the surface, as seen in Fig. 4.

3.3. Tensile properties

Engineering stress-engineering strain and engineering stress-displacement curves for LB-PBF Al alloys investigated in this study are presented in Fig. 6(a) and (b). Besides, the quasi-static tensile properties including yield strength, S_y, ultimate tensile strength, S_u, modulus of elasticity, E, percent elongation, %El, true fracture strain or ductility, ε_f, and percent reduction in area, %RA, for all the Al alloys examined in this study are listed in Table 4 and shown in Fig. 7.

In addition, the tensile properties of wrought [43] and LB-PBF [44] A356 alloy (both in NHT and T6 conditions), as well as wrought [45] and LB-PBF [46] AA6061 alloy (both in NHT and T6 conditions), are included in Table 4 for comparison. As seen, the LB-PBF LPW and EOS AlSi10Mg alloys possess comparable, and the LB-PBF Scalmalloy and LB-PBF QuesTek Al have significantly higher tensile strengths (i.e., S_y and S_u) as compared to those of the wrought and LB-PBF A356 and AA6061 alloys both in NHT and T6 conditions. In terms of ductility, LB-PBF LPW AlSi10Mg and Scalmalloy have higher, EOS AlSi10Mg has comparable,
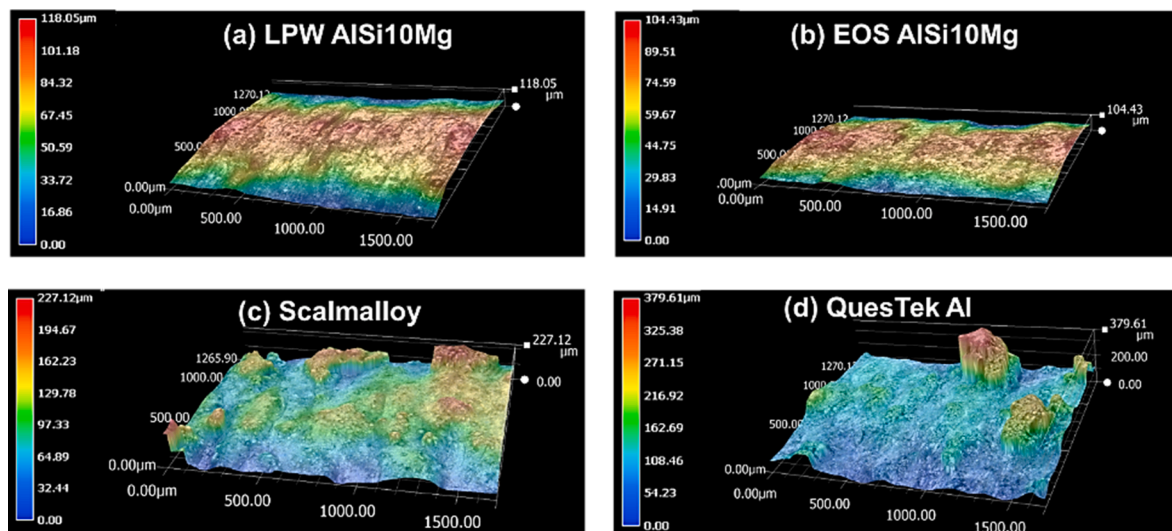

Fig. 4. Representative surface roughness profiles of the LB-PBF Al alloys with the as-built surface condition: (a) LPW AlSi10Mg, (b) EOS AlSi10Mg, (c) Scalmalloy, and (d) QuesTek Al.
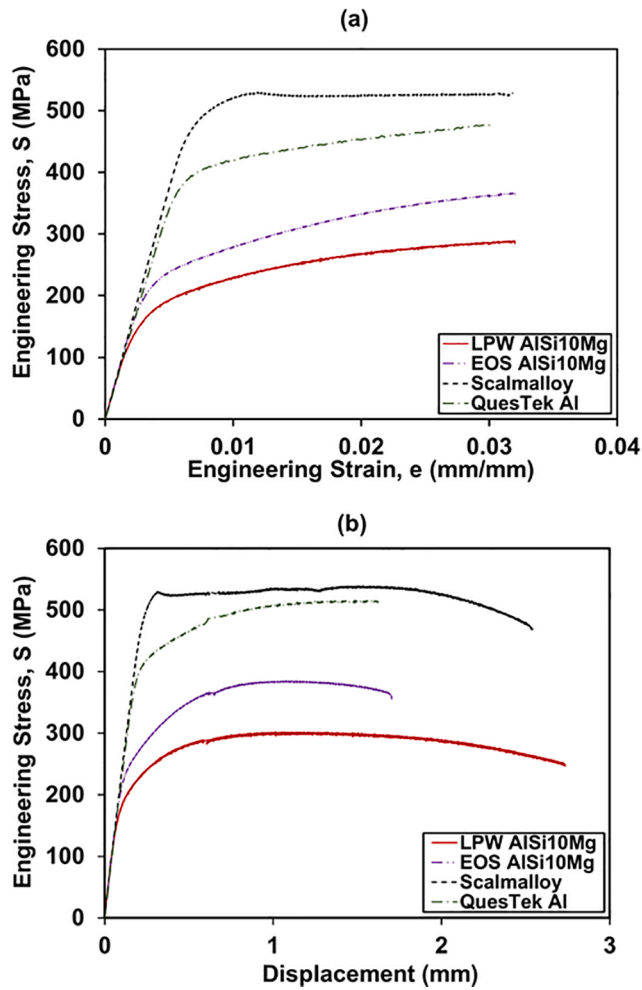
Fig. 6. Tensile behavior of LB-PBF Al alloys: (a) engineering stress-engineering strain curves, and (b) engineering stress-displacement curves.

Table 4
Tensile properties of LB-PBF Al alloys investigated in this study, wrought [43] and LB-PBF [44] A356, as well as wrought [45] and LB-PBF [46] AA6061 alloys.

Alloy	Heat treatment	S_y (MPa)	S_u (MPa)	E (GPa)	% El	ε_f	% RA
LB-PBF LPW AlSi10Mg	Stress-relieved	189	302	74	19	0.48	38
LB-PBF EOS AlSi10Mg	Stress-relieved	246	366	78	12	0.17	15
LB-PBF Scalmalloy	325 °C, 4 h	508	530	77	16	0.44	35
LB-PBF QuesTek Al	185 °C, 2 h	421	496	77	5	0.06	6
Wrought A356	T6	195	228	–	2	–	–
LB-PBF A356	NHT	228	384	–	13	–	–
LB-PBF A356	T6	210	270	–	13	–	–
Wrought AA6061	NHT	55	124	–	30	–	–
Wrought AA6061	T6	276	310	–	12	–	–
LB-PBF AA6061	NHT	71	137	–	13	–	–
LB-PBF AA6061	T6	286	313	–	4.5	–	–

and QuesTek Al has lower *%El* to those of wrought A356 and AA6061 alloys in T6 condition.

The variation in the tensile properties among the four LB-PBF Al alloys investigated herein (see Fig. 6 and Table 4) can be attributed to the differences in their microstructure. The LB-PBF Scalmlloy possesses the highest tensile strength (i.e., S_y and S_u), and considerably high ductility among the LB-PBF Al alloys, which may be ascribed to its ultrafine/nano-size grain structure (see Fig. 2(c) as well as precipitation hardening behavior of the material [22,47]. Although the LB-PBF QuesTek Al also has high tensile strength, it is the least ductile material among all the LB-PBF alloys investigated in this study. The high tensile strength of LB-PBF QuesTek Al can be attributed to its fine grain structure (see Fig. 2(d) and the possible formation of SiO_2 phase (see Fig. 3(d)) in the microstructure. It has been shown that the formation of the SiO_2 phase increases the strength of Al alloys, which is in agreement with the findings of [48]. The tensile fracture behavior is elaborated further in Section 4.1.

For the LB-PBF AlSi10Mg alloy, different tensile properties are obtained for the LPW and EOS batches. Although the LB-PBF LPW and EOS AlSi10Mg alloys have similar grain structures (see Fig. 2(a) and (b), respectively), the EOS AlSi10Mg has higher tensile strength (~23% higher S_y and ~17% higher S_u) and lower ductility (~37%) than the LPW AlSi10Mg. Such variations may be attributed to the slight differences in their chemical composition (see Table 1) as well as post thermal heat treatment (see Table 3), which may have resulted in different microstructures.

3.4. Cyclic deformation and fatigue behavior

The stable stress–strain hysteresis loops of the fully-reversed strain-controlled fatigue tests for the machined LB-PBF Al specimens are presented in Fig. 8. From the cyclic stress–strain relationship shown, it is noticeable that both the LB-PBF LPW and EOS AlSi10Mg alloys exhibit considerable plastic deformation at 0.0050 mm/mm strain amplitude, while the cyclic deformation behavior of the LB-PBF Scalmalloy and LB-PBF QuesTek Al is elastic.

As seen in Fig. 8(a) and (b) for the LB-PBF LPW and EOS AlSi10Mg alloys, the cyclic stress response at 0.0030 mm/mm and 0.0050 mm/mm strain amplitudes are close or higher than the S_y of the material (see Table 4); therefore, these alloys have considerable amount of plastic deformation at these strain amplitudes. Moreover, the LB-PBF EOS AlSi10Mg has thinner hysteresis loops representing lower plasticity than the LB-PBF LPW AlSi10Mg. This may be explained by the higher strength and lower ductility of the LB-PBF EOS AlSi10Mg (see Fig. 6, Fig. 7, and Table 4) as compared to the LB-PBF LPW AlSi10Mg.

The fatigue data of LB-PBF Al alloys consisting of strain amplitude, ε_a, elastic strain amplitude, $\frac{\Delta\varepsilon_e}{2}$, plastic strain amplitude, $\frac{\Delta\varepsilon_p}{2}$, mid-cycle stress amplitude, σ_a, mid-cycle mean stress, σ_m, and reversals to failure, $2N_f$, for specimens in as-built and machined surface conditions are listed in Table 5 and Table 6, respectively. The plastic strain amplitude for each specimen was calculated by subtracting the elastic strain amplitude from the total strain amplitude. It is notable that most of the specimens in this study experienced tensile/compressive mean stress less than 10% of the stress amplitude, which should not impact their fatigue behavior to a considerable extent. It is worth mentioning that the $\sqrt{area}$ of exact defects size as well as the type of defects initiating the crack on the fracture surface of all the machined specimens are also included in Table 6. The volumetric defects located at or adjacent to the surface are considered as "*surface pore/LoF*", while the ones located at a distance equal to, or greater than the corresponding defect's $\sqrt{area}$, from the surface are considered as "*internal pore/LoF*". Cracks in the specimens with as-built surface condition were observed to all initiate from the surface micro-notches.

To better understand the elastic and plastic behavior of the LB-PBF Al specimens, elastic and plastic strain amplitudes of as-built and machined surface specimens were used to calculate the strain-life properties [49] based on the following equation (comprising of the Basquin and Coffin-Manson equations):
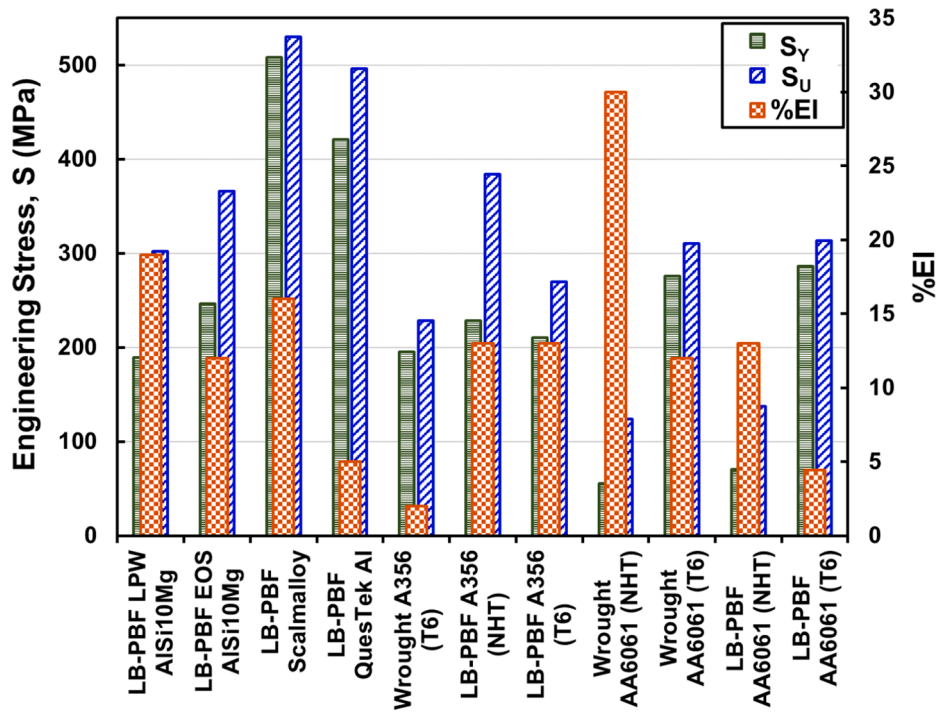
Fig. 7. Column chart presentation of the tensile properties of LB-PBF Al alloys investigated in this study, as well as wrought [43] and LB-PBF [44] A356, and wrought [45] and LB-PBF [46] AA6061 alloys from literature.
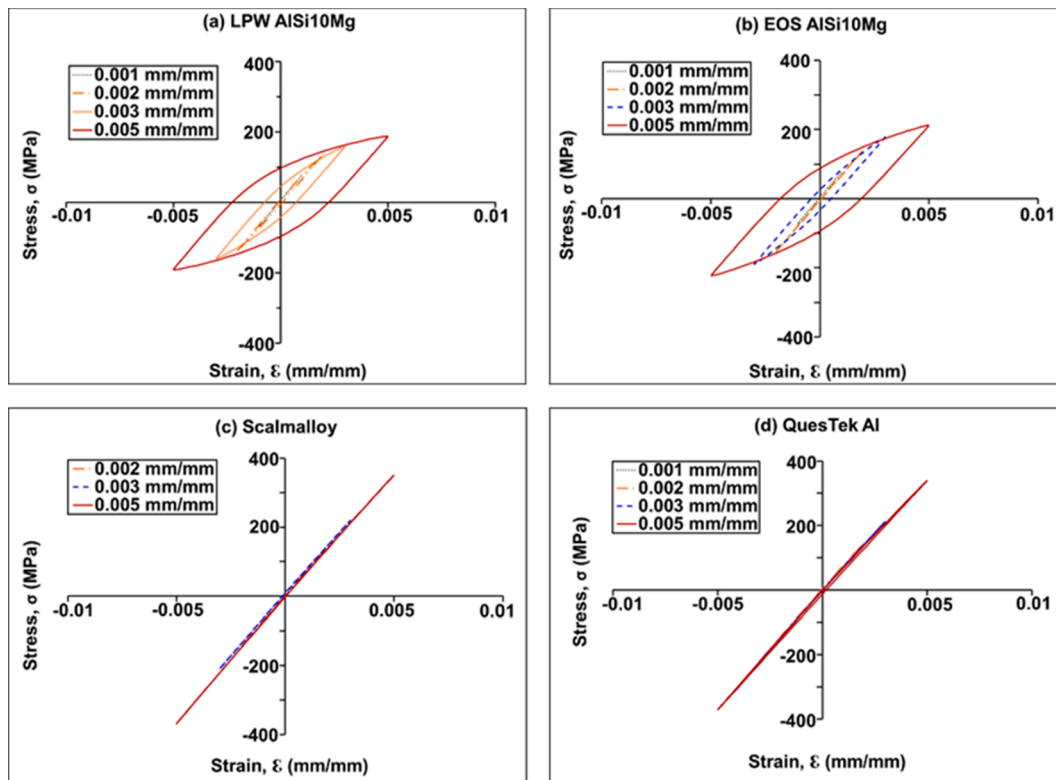
Fig. 8. Stable hysteresis loops of uniaxial fully-reversed strain-controlled fatigue tests for the LB-PBF Al specimens with the machined surface condition: (a) LPW AlSi10Mg, (b) EOS AlSi10Mg, (c) Scalmalloy, and (d) QuesTek Al.

$$\frac{\Delta \varepsilon}{2} = \varepsilon_a = \frac{\Delta \varepsilon_e}{2} + \frac{\Delta \varepsilon_p}{2} = \frac{\sigma_f'}{E}(2N_f)^b + \varepsilon_f'(2N_f)^c$$

where E is the modulus of elasticity, σ_f' is the fatigue strength coefficient,

ε_f' is the fatigue ductility coefficient, and b and c are the fatigue strength and fatigue ductility exponents, respectively. The fatigue properties (i. e., σ_f', ε_f', b, and c) of the LB-PBF Al alloys for both as-built and machined

Table 5
Uniaxial fully-reversed strain-controlled fatigue data of the LB-PBF Al specimens with the as-built surface condition.

Alloy	ID	ε_a (mm/mm)	$\frac{\Delta\varepsilon_e}{2}$ (mm/mm)	$\frac{\Delta\varepsilon_p}{2}$ (mm/mm)	σ_a (MPa)	σ_m (MPa)	$2N_f$ (Reversals)
LPW AlSi10Mg	A39	0.0030	0.0024	0.0006	177	−12	11,264*
	A35	0.0030	0.0025	0.0005	177	−19	15,586
	A16	0.0020	0.0019	0.0001	138	2	40,000
	A22	0.0020	0.0019	0.0001	140	−12	66,916
	A40	0.0010	0.0010	0	76	11	601,168
	A32	0.0010	0.0010	0	73	7	961,504
	A04	0.00075	0.00075	0	57	−3	>10,000,000
	A29	0.00075	0.00075	0	56	−6	>10,000,000
EOS AlSi10Mg	Al10	0.0030	0.0025	0.0005	177	−9	14,194
	Al07	0.0030	0.0024	0.0006	178	−13	14,704
	Al36	0.0020	0.0019	0.0001	142	−10	73,672
	Al01	0.0020	0.0019	0.0001	141	−1	79,562
	Al32	0.0010	0.0010	0	78	4	729,154
	Al40	0.0010	0.0010	0	79	−4	1,017,592
	Al39	0.00075	0.00075	0	58	0	>10,000,000
	Al43	0.00075	0.00075	0	57	−1	>10,000,000
Scalmalloy	B42	0.0030	0.0030	0	204	−1	29,056
	B19	0.0030	0.0030	0	215	3	37,070
	B29	0.0020	0.0020	0	146	−4	122,342
	B22	0.0020	0.0020	0	136	−4	127,848
	B39	0.0010	0.0010	0	72	0	431,968
	B25	0.0010	0.0010	0	70	−1	470,710
	B16	0.00075	0.00075	0	56	1	>10,000,000
	B32	0.00075	0.00075	0	54	5	>10,000,000
QuesTek Al	C29	0.0030	0.0030	0	218	−2	4,952
	C39	0.0030	0.0030	0	210	−12	9,710
	C36	0.0020	0.0020	0	138	−1	17,160
	C42	0.0020	0.0020	0	141	0	31,074
	C07	0.0010	0.0010	0	72	0	142,000
	C19	0.0010	0.0010	0	76	−3	198,012
	C22	0.00075	0.00075	0	56	0	306,928
	C10	0.00075	0.00075	0	55	2	428,728

* Cracks in all the as-built surface specimens initiated from surface micro-notches.

surface conditions are listed in Table 7. The main parameters of Coffin-Manson equation, i.e., ε_f' and c, for the Scalmalloy and QuesTek Al are zero due to the lack of plastic deformation in these alloys for strain levels examined in this study. Therefore, only Basquin parameters, σ_f' and b, of the strain-life properties are reported for these alloys in Table 7. On the other hand, the Coffin-Manson parameters in Table 7 for the LPW and EOS AlSi10Mg are not zero due to the measurable plastic deformations in these materials. It is worth mentioning that the runout specimens were not considered in these calculations.

In addition, the strain-life fatigue behavior of LB-PBF Al specimens in as-built surface and machined surface conditions are presented in Fig. 9. As seen, removing the surface roughness by machining increases the fatigue resistance of the material, which has also been shown for other AM materials [50]. However, depending on the surface roughness severity in the as-built surface condition as compared to that of the machined condition, as well as the level of plastic deformation in the material, improvement in fatigue resistance may vary. It is worth mentioning that the as-built LB-PBF Al specimens, except the QuesTek Al ones, reach runout level at 0.00075 mm/mm strain amplitude. For machined LB-PBF Al specimens, the LPW and EOS AlSi10Mg, as well as QuesTek Al, reach runout at 0.0010 mm/mm strain amplitude, while the runout level for the Scalmalloy specimens is 0.0020 mm/mm. This confirms the superior fatigue performance of Scalmalloy to other investigated Al alloys.

It can be noticed that the LB-PBF LPW and EOS AlSi10Mg alloys have somewhat similar fatigue resistance in the as-built and machined surface conditions with a slight increase of fatigue life for the machined specimens, while the enhancement in fatigue lives of the Scalmalloy and QuesTek Al specimens in machined surface conditions is much more evident. This is due to the high surface roughness of the Scalmalloy and QuesTek Al specimens, and the lack of plastic deformation alleviated the fatigue resistance of the material significantly; therefore, removing the

surface roughness resulted in a considerable improvement in their fatigue performance. Moreover, it should be noted that the fatigue performance of LB-PBF Scalmalloy and QuesTek Al specimens with the as-built surface condition may have been exacerbated even further due to their high surface roughness resulting from the non-optimized contour parameters.

4. Discussion on experimental results

In this section, the tensile behavior of the LB-PBF LPW AlSi10Mg, EOS AlSi10Mg, Scalmalloy, and QuesTek Al alloys are discussed by explaining their behavior based on their micro-/defect-structures. In addition, their fatigue properties are compared in as-built and machined surface conditions, and the failure mechanisms are revealed by investigating the fracture surfaces.

4.1. Tensile behavior and the role of microstructure

Among the LB-PBF Al alloys investigated in this study, the Scalmalloy possesses the highest tensile strength (i.e., S_y, and S_u) as compared to the other alloys, while also exhibiting high ductility as seen in Fig. 6. Although the QuesTek Al has high strength (S_y = 421 MPa and S_u = 496 MPa) compared to LB-PBF AlSi10Mg, its ductility is significantly lower ($\%El_{QuesTek Al}$ = 5, $\%El_{EOS AlSi10Mg}$ = 12, $\%El_{LPW AlSi10Mg}$ = 19). Regarding the LB-PBF AlSi10Mg alloy, the specimens fabricated with the EOS powder exhibit higher tensile strength but lower ductility than those fabricated with the LPW powder; this may be attributed to a slight difference in their stress-relieving procedures.

The variation in the mechanical properties of the Al alloys examined in this study is associated with the differences in their microstructure, mainly the grain size, as well as the presence of secondary phases/precipitates. According to the Hall-Petch relationship [51], the yield strength, S_y, is inversely related to the grain size, meaning that S_y

Table 6
Uniaxial fully-reversed strain-controlled fatigue data of the LB-PBF Al specimens with the machined surface condition.

Alloy	ID	ε_a (mm/mm)	$\frac{\Delta\varepsilon_e}{2}$ (mm/mm)	$\frac{\Delta\varepsilon_p}{2}$ (mm/mm)	σ_a (MPa)	σ_m (MPa)	$2N_f$ (Reversals)	$\sqrt{area}$ of defect(s) (μm)	Defect location and types
LPW AlSi10Mg	A'20	0.0050	0.0029	0.0021	201	1	5,246	38, 35	Surface LoFs*
	A'17	0.0050	0.0029	0.0021	202	−1	7,358	34, 26	Surface LoFs
	A'02	0.0030	0.0024	0.0006	172	−3	21,348	70, 30	Surface LoFs
	A'38	0.0030	0.0024	0.0006	170	−1	23,116	37	Surface LoF
	A'15	0.0020	0.0020	0	139	0	140,840	49	Surface LoF
	A'18	0.0020	0.0020	0	137	−2	146,256	57	Surface LoF
	A'28	0.0010	0.0010	0	73	−6	>10,000,000	–	–
	A'23	0.0010	0.0010	0	73	5	>10,000,000	–	–
EOS AlSi10Mg	Al'31	0.0050	0.0032	0.0018	237	−4	6,140	37	Surface pore
	Al'30	0.0050	0.0033	0.0017	238	−4	6,144	45	Internal LoF
	Al'46	0.0030	0.0027	0.0003	200	−9	29,372	47	Surface LoF
	Al'11	0.0030	0.0026	0.0004	196	−7	34,026	50	Surface pore
	Al'02	0.0020	0.0020	0	154	6	149,642	41	Surface LoF
	Al'37	0.0020	0.0020	0	154	4	161,296	74	Surface pore
	Al'12	0.0020	0.0020	0	149	−5	362,850	45	Surface LoF
	Al'23	0.0010	0.0010	0	74	1	>10,000,000	–	–
	Al'15	0.0010	0.0010	0	74	4	>10,000,000	–	–
Scalmalloy	B'46	0.0050	0.0050	0	363	−7	16,186	36	Surface pore
	B'15	0.0050	0.0050	0	358	−9	20,366	52	Surface pore
	B'30	0.0030	0.0030	0	217	4	71,488	41	Surface LoF
	B'13	0.0030	0.0030	0	218	−5	160,152	36	Surface LoF
	B'02	0.0030	0.0030	0	212	6	183,086	157	Internal LoF
	B'23	0.0020	0.0020	0	145	3	>10,000,000	–	–
	B'38	0.0020	0.0020	0	145	1	>10,000,000	–	–
QuesTek Al	C'17	0.0050	0.0050	0	359	−13	4,012	41, 34	Surface LoF, Internal LoF
	C'23	0.0050	0.0050	0	358	−15	5,004	54	Surface LoF
	C'28	0.0030	0.0030	0	220	0	59,778	54, 39	Surface LoF, Internal LoF
	C'02	0.0030	0.0030	0	220	−7	61,778	89	Surface LoF
	C'15	0.0020	0.0020	0	147	0	170,596	92	Surface LoF
	C'18	0.0020	0.0020	0	146	−1	633,740	75	Surface LoF
	C'37	0.0010	0.0010	0	71	0	>10,000,000	–	–
	C'27	0.0010	0.0010	0	72	−1	>10,000,000	–	–

* Cracks initiated from defects located at or adjacent to the surface are defined as "*Surface pore/LoF*", while the cracks initiated from defects with a distance equal to, or greater than the corresponding defect's $\sqrt{area}$ from the surface are defined as "*internal pore/LoF*".

Table 7
Fatigue properties of LB-PBF Al alloys with as-built and machined surface conditions.

Surface condition	Alloy	σ'_f (MPa)	b	ε'_f (mm/mm)	c
As-built	**LPW AlSi10Mg**	474	−0.115	0.358	−0.689
	EOS AlSi10Mg	508	−0.119	0.274	−0.651
	Scalmalloy	1058	−0.172	–	–
	QuesTek Al	630	−0.151	–	–
Machined	**LPW AlSi10Mg**	585	−0.124	0.635	−0.663
	EOS AlSi10Mg	751	−0.132	0.286	−0.596
	Scalmalloy	1274	−0.140	–	–
	QuesTek Al	863	−0.120	–	–

increases as the grain size decreases. Therefore, one reason for the high S_y of the LB-PBF Scalmalloy is the presence of ultrafine/nano-size grains in its microstructure (Fig. 2(c)). Similarly, the LB-PBF QuesTek Al possesses higher S_y than LB-PBF LPW and EOS AlSi10Mg alloys due to its finer grain structure (see Fig. 2(e)).

The strength of Al alloys also can be increased due to the formation of various precipitates [52]. Fig. 10 presents the ECCI micrographs of the LB-PBF Al alloys obtained using a BSD detector to characterize the secondary phases. Comparing the microstructure of LB-PBF LPW AlSi10Mg (Fig. 10(a)) with that of the LB-PBF EOS AlSi10Mg (Fig. 10(b)), the latter has a fine cellular structure (average cell size of ~1 μm), while there is no sign of cell structures in the microstructure of LPW AlSi10Mg. Due to the high cooling rate during the LB-PBF process, fine

cellular structures with the intercellular Si networks can form in the AlSi10Mg, which increases the strength and reduces the ductility of the material [36,37]. However, by performing a proper post heat treatment on LB-PBF AlSi10Mg, the Si networks are dissolved, and fine Si particles are formed in the Al matrix [53].

The intercellular Si networks, which normally form during the manufacturing, still exist in the microstructure of the LB-PBF EOS AlSi10Mg (shown by yellow arrows in Fig. 10(b)), while there are fine Si particles dispersed in the microstructure of the LB-PBF LPW AlSi10Mg (shown by yellow arrows in Fig. 10(a)). This may be attributed to the fact that the LB-PBF LPW AlSi10Mg was subjected to a higher stress-relieve temperature and longer duration than what was applied to the LB-PBF EOS AlSi10Mg. As a result of the intercellular Si networks dissolution, the LB-PBF LPW AlSi10Mg exhibits lower tensile strength and higher ductility than the EOS counterpart (see Fig. 6).

The fine grains of the LB-PBF Scalmalloy and the almost uniform dispersion of nano-size $Al_3(Sc,Zr)$ precipitates shown by red arrows are evident in Fig. 10(c). This can also be confirmed by the EDS maps of Sc and Zr, presented in Fig. 3(c). These coherent nano-size precipitates formed both during the fabrication and the post heat treatment, can increase the strength of the material. Therefore, the high strength of the LB-PBF Scalmalloy can be attributed to both ultrafine/nano-size grains (based on Hall-Petch relationship) as well as the formation of $Al_3(Sc,Zr)$ precipitates in the microstructure during both the fabrication and the heat treatment. For the QuesTek Al, the dendritic cellular structure (shown by blue arrows in Fig. 10(d)) and possibly the formation of the SiO_2 phases (see Fig. 3(d)) may be the reasons for the high strength of this material; it has been shown that high dislocation density in the cellular structures can increase the strength in some materials [54].

The tensile fracture surfaces along with the EDS maps of the LB-PBF Al alloys, are presented in Fig. 11. Volumetric defects, such as pores and
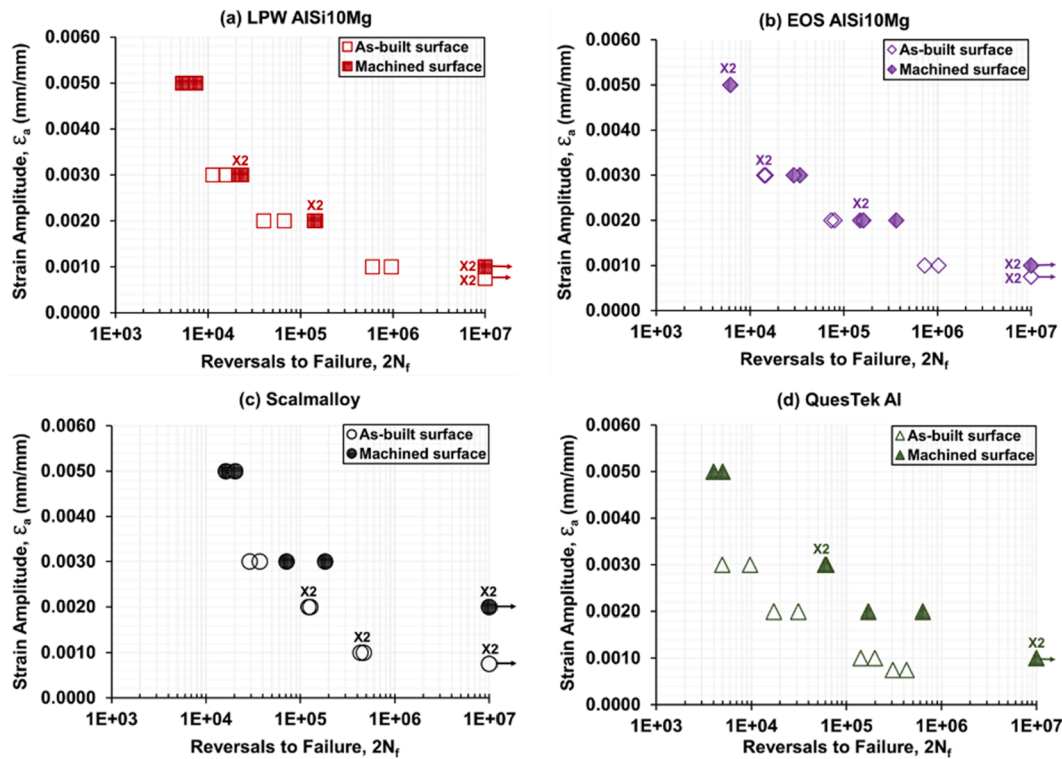
Fig. 9. The comparison of strain-life fatigue behavior of specimens in as-built and machined surface conditions: (a) LPW AlSi10Mg, (b) EOS AlSi10Mg, (c) Scalmalloy, and (d) QuesTek Al.

LoFs, are shown by yellow arrows on the fracture surfaces of the specimens. The fracture surface of an LPW AlSi10Mg specimen, shown in Fig. 11(a), represents a ductile behavior comprising dimples shown by white arrows. However, the facets seen on the fracture surface of the EOS AlSi10Mg specimen (marked by black arrows in the magnified image in Fig. 11(b)) imply a more brittle fracture for the LB-PBF EOS AlSi10Mg as compared to the LPW counterpart.

Moreover, as observed in EDS maps of Fig. 11(b), there are large oxide inclusions on the fracture surface of the EOS AlSi10Mg specimen. These oxide inclusions, which may have formed because of the presence of O gas in the chamber (although the O content is very low in the chamber, Al is very reactive and the spattered particles may be oxidized) or the oxide layer on the powder particles, can reduce the ductility of the material. The fibrous fracture surface of LB-PBF Scalmalloy can be observed in Fig. 11(c), which includes both fine as well as large and deep dimples, representing the ductile rupture of this material. On the other hand, the fracture surface of LB-PBF QuesTek Al is comprised of cleavage facets shown by black arrows, revealing the low ductility of this material. This low ductility may be attributed to the formation of the brittle SiO_2 phase in the microstructure of QuesTek Al (see Fig. 3(d)) [48].

4.2. Fatigue behavior and failure mechanisms

4.2.1. Effects of As-built surfaces

The strain-life and stress-life fatigue data of the LB-PBF Al specimens with the as-built surface condition are shown in Fig. 12(a) and (b). It has been well established that the surface roughness causes the stress concentration on the surface, potentially resulting in swifter crack initiations [55]. There are several studies that have shown multiple crack initiations from micro-notches on the rough surface of as-fabricated AM parts, which deteriorate their fatigue performance [7,55].

The LB-PBF LPW and EOS AlSi10Mg specimens with similar surface roughness values (i.e., R_a, R_v, and R_t), as shown in Fig. 5, exhibit similar fatigue resistance in Fig. 12, although there are differences in their

microstructure and tensile properties. The LB-PBF QuesTek Al has the worst fatigue behavior among the other alloys, mostly because it has the highest surface roughness value ($R_a = \sim24$ μm, $R_v = \sim37$ μm, $R_t = \sim143$ μm). It should be reminded that the surface process parameters (i.e., contour) of Scalmalloy and QuesTek Al were not optimized. Hence, the Scalmalloy and QuesTek Al specimens have much higher surface roughness values as compared to the AlSi10Mg specimens. Therefore, considering its high strength and low ductility, the LB-PBF QuesTek Al is more sensitive to the surface defects under cyclic loading.

On the other hand, although the LB-PBF Scalmalloy specimens also have a high surface roughness ($R_a = \sim19$ μm, $R_v = \sim29$ μm, $R_t = \sim86$ μm), they outperform the fatigue resistance of the LB-PBF QuesTek Al. This is due to the ultrafine/nano-size grain structure as well as the presence of coherent nano-size precipitates in the microstructure of Scalmalloy. Interestingly, while having much higher surface roughness, the LB-PBF Scalmalloy has superior fatigue performance as compared to the LB-PBF LPW and EOS AlSi10Mg alloys in the LCF and mid-cycle fatigue (MCF) regimes. This superior fatigue performance of Scalmalloy can be attributed to its higher strength and ductility compared to those of LPW and EOS AlSi10Mg, which can potentially increase the fatigue crack growth life. It is well known that the fatigue crack growth life consists of a considerable portion of overall fatigue life in LCF as compared to the HCF regime [49].

In the HCF regime, the LB-PBF Scalmalloy exhibits comparable fatigue performance to the LB-PBF LPW and EOS AlSi10Mg alloys, which can be explained by the much higher surface roughness of Scalmalloy specimens. The reduction in fatigue resistance of the Scalmalloy specimens in the as-built surface condition in HCF is attributed to the non-optimized surface process parameters used for fabrication. There are studies reporting the superior fatigue resistance of the LB-PBF Scalmalloy to those of the LB-PBF AlSi10Mg in the as-fabricated surface condition [29]. Therefore, it is expected that the fatigue performance of Scalmalloy to improve, specifically in the HCF regime, if optimized surface parameters are used during the LB-PBF fabrication.

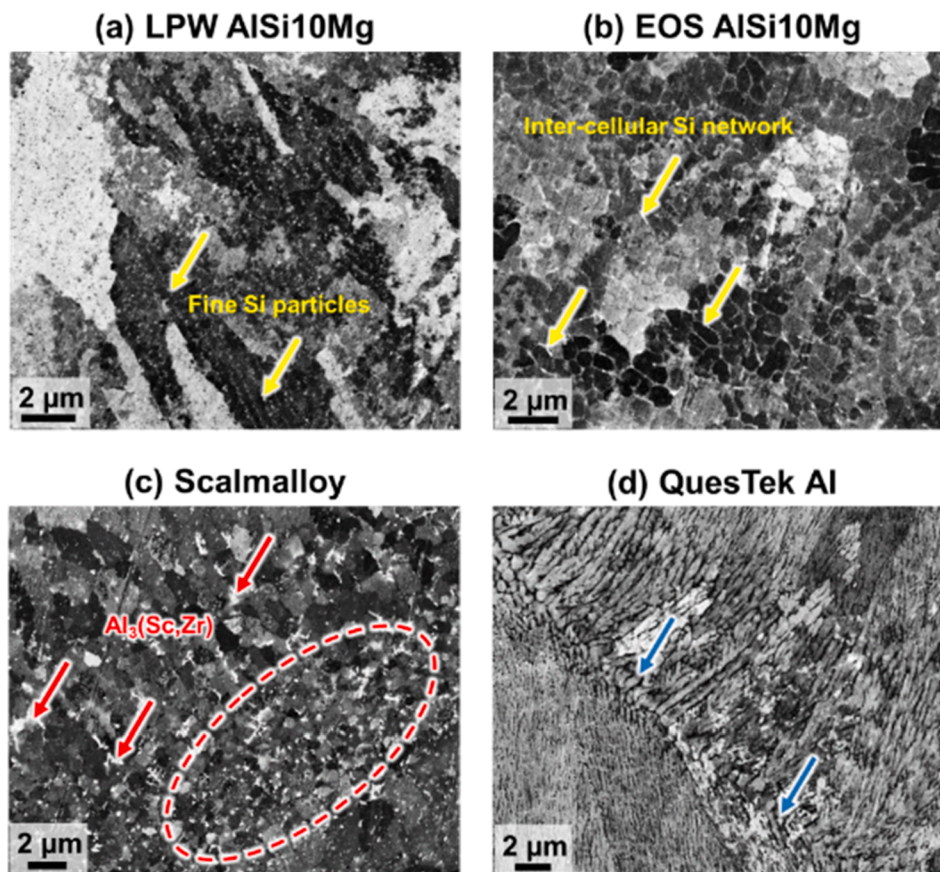To understand the failure mechanisms of the LB-PBF Al Alloys in the

Fig. 10. The ECCI micrographs of the LB-PBF Al alloys: (a) LPW AlSi10Mg, (b) EOS AlSi10Mg, (c) Scalmalloy, and (d) QuesTek Al. Note that the yellow arrows in (a) and (b) point at the Si particles/network, the red arrows in (c) point at the $Al_3(Sc,Zr)$ particles, and the blue arrows in (d) point at the dendritic cellular structure. (For interpretation of the references to colour in this figure legend, the reader is referred to the web version of this article.)

as-built surface condition, a selected fracture surface for each alloy tested at 0.0020 mm/mm strain amplitude is shown in Fig. 13. The lower surface roughness of LPW and EOS AlSi10Mg specimens can be noticed in Fig. 13(a) and (b), which is ascribed to the optimized process parameters used for these specimens. However, there are un-melted/partially melted powder particles attached to the surfaces of the LB-PBF Scalmalloy and LB-PBF QuesTek Al specimens, showing the fact that the surface process parameters were not optimized for them. Nonetheless, the cracks started from the micro-notches on the surface in all of these specimens. In addition, white ridges indicated by blue arrows represent the coalescence of the cracks that originated from different locations (and sometimes different layers) on the surface. The black arrows in the fracture surfaces of Fig. 13 are indicating the final fracture areas.

For the LB-PBF EOS AlSi10Mg specimen tested at 0.0020 mm/mm strain amplitude, it can be seen from Fig. 13(b) that multiple cracks have been initiated from different layers, while one crack has initiated from an LoF defect adjacent to the surface. After nucleation from different planes, these multiple cracks smoothly propagated and ultimately coalesced, followed by the final fracture. A similar observation has been reported for LB-PBF AlSi10Mg specimens with the as-built surface roughness in the literature at both room and elevated temperatures [56]. Therefore, if the surface roughness is sufficiently low, or there are relatively large volumetric defects, specifically LoF ones close to the surface, the cracks may also initiate from the volumetric defects [57,58].

4.2.2. Effects of microstructure and volumetric defects

The strain-life and stress-life fatigue data of machined LB-PBF Al specimens investigated in this study are shown in Fig. 14(a) and (b). As was expected, the Scalmalloy specimens in machined surface condition

exhibit significantly higher fatigue lives as compared to other alloys in both HCF (more than two orders of magnitude longer than other alloys) and LCF (one order of magnitude longer fatigue lives than other alloys) regimes. Considering the high tensile strength and ductility of the Scalmalloy due to the ultrafine/nano-size grain structure (see Fig. 2) and the presence of coherent precipitates i.e., $Al_3(Sc,Zr)$, the fatigue resistance of this material is improved in all regimes after removing the surface roughness via machining. It is also worth noting that due to the high strength of Scalmalloy and QuesTek Al, they have significantly higher cyclic stress responses than those of LPW and EOS AlSi10Mg specimens (see Fig. 14(b)).

There is scatter in the fatigue results of the QuesTek Al in HCF regime, which can be explained by its high strength and low ductility (due to the presence of dendritic cellular structure and brittle SiO_2 phases), making it more susceptible to the presence of volumetric defects in the absence of plastic deformation [55]. In addition, it is worth mentioning that the stress responses of machined LB-PBF EOS AlSi10Mg specimens are slightly higher than the machined LPW AlSi10Mg specimens (see Fig. 14(b)) at the same strain amplitudes. This discrepancy in cyclic stress response might be attributed to their differences in microstructure resulting from different heat treatments as well as different chemical compositions, as discussed in Sections 2.2, 3.1, and 3.4.

Typically, the volumetric defects (i.e., pores, LoF) are responsible for the crack initiation in AM materials with the machined surface condition [50,59]. The shape, size, and location (with respect to the surface boundary of the specimen) of the volumetric defects are also influential on the final fatigue life [60]; the larger and the closer the defects are to the surface, the shorter the fatigue life typically is. However, there are some AM materials (e.g., Inconel 718 [61,62], 304L stainless steel [63]) when fabricated employing optimized process parameters, the cracks
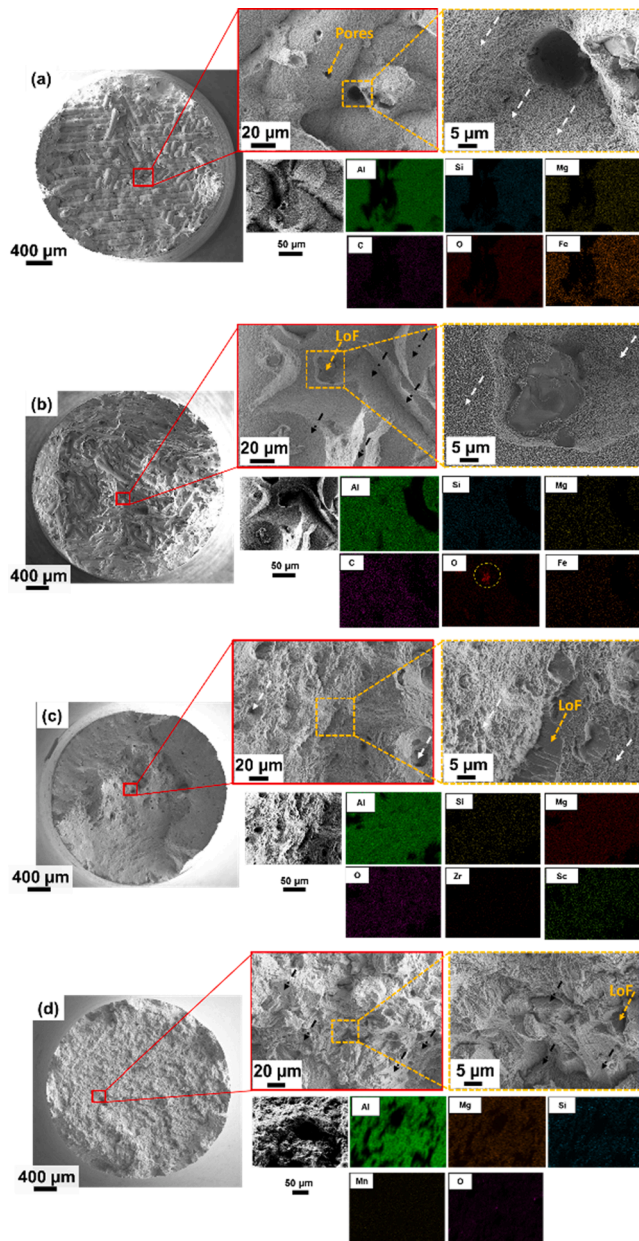
Fig. 11. Tensile fracture surfaces of the LB-PBF Al Alloys: (a) LPW AlSi10Mg, (b) EOS AlSi10Mg, (c) Scalmalloy, and (d) QuesTek Al. Note that the yellow arrows point at the pores/LoF defects, black arrows point at facets, and white arrows point at the dimples. (For interpretation of the references to colour in this figure legend, the reader is referred to the web version of this article.)

typically initiate from the surface or microstructure features (e.g., facets, twins, etc.) with the reduction of detrimental volumetric defects.

To better understand the fatigue failure mechanisms in LB-PBF Al alloys with the machined surface condition, fractography analysis is carried out on all the specimens. It was observed that the cracks initiated from the volumetric defects, either pores or LoF, in all cases. The $\sqrt{area}$ of exact defect sizes as well as the type of defects are listed in Table 6. The average $\sqrt{area}$ of defects that initiated the cracks for the LPW AlSi10Mg, EOS AlSi10Mg, Scalmalloy, and QuesTek Al specimens are calculated to be 43 μm, 49 μm, 64 μm, and 60 μm, respectively.

In general, the QuesTek Al machined specimens have larger $\sqrt{area}$ of defects as compared to the other alloys. This is due to the fact that the process parameters used to fabricate this alloy were not necessarily the most optimized set. However, an optimized set of process parameters
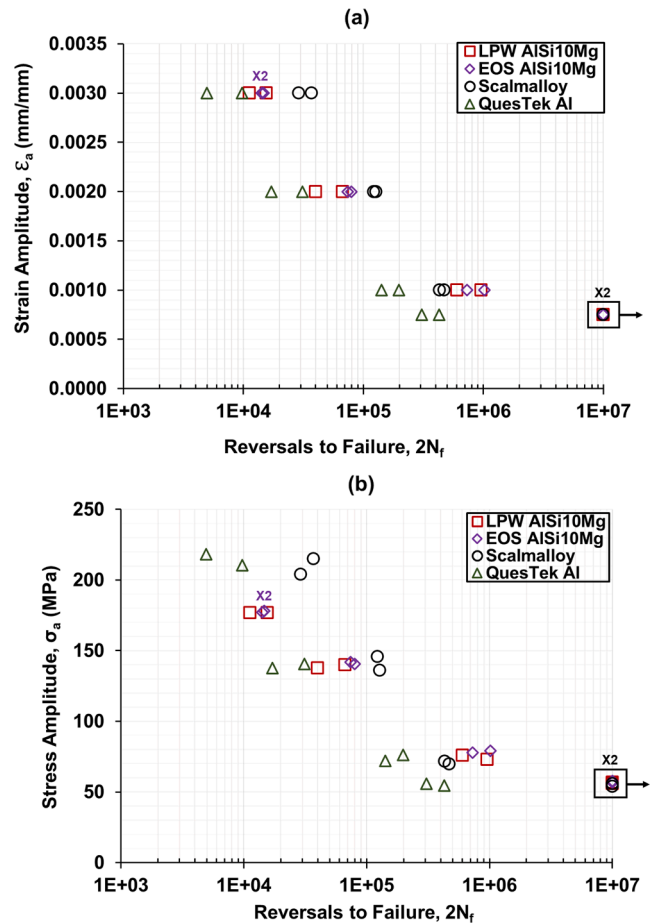

Fig. 12. (a) Strain-life and (b) stress-life fatigue data of LB-PBF Al specimens in as-built surface condition.

were used to fabricate the LPW and EOS AlSi10Mg specimens, and accordingly, these specimens have very similar $\sqrt{area}$ of defects and much smaller than the ones for the QuesTek Al specimens. For the LB-PBF Scalmalloy machined specimens, most of the defects which have initiated the cracks are not very large and are somewhat comparable to those of AlSi10Mg machined specimens (see Table 6). It is worth noting that there is only one specimen characterized by a relatively large internal LoF defect (specimen B'02), which is the reason for Scalmalloy having a relatively high average $\sqrt{area}$ of defects (i.e., 64 μm). Therefore, the process parameters used for the Scalmalloy in this study might be close to an optimized set.

The fracture surfaces of selected machined LB-PBF Al specimens tested at 0.0030 mm/mm strain amplitude, which corresponds to the MCF regime, are shown in Fig. 15. It can be seen in Fig. 15(a) for the LPW AlSi10Mg specimen that surface LoF defects with $\sqrt{area}$ of 70 μm, and 30 μm (specimen A'02 with 21,348 reversals to failure) initiated the cracks, while the $\sqrt{area}$ of the surface LoF defect that initiated the crack in the EOS AlSi10Mg (Fig. 15(b)) is 47 μm (specimen Al'46 with 29,372 reversals to failure).

Although it is expected for the LPW AlSi10Mg specimen (i.e., specimen A'02) to have a considerably shorter fatigue life due to multiple crack initiation defects, its fatigue performance is comparable to that of EOS AlSi10Mg counterpart (i.e., specimen Al'46). It is also notable for the LB-PBF AlSi10Mg machined specimens tested at 0.0050 mm/mm strain amplitude (i.e., LCF regime) that although multiple defects initiated the cracks in LPW AlSi10Mg specimens (e.g., specimens ID A'17 and A'20), almost similar fatigue lives were obtained as compared to the EOS AlSi10Mg counterparts (e.g., specimens ID Al'31 and Al'30) in which only one defect initiated the crack.
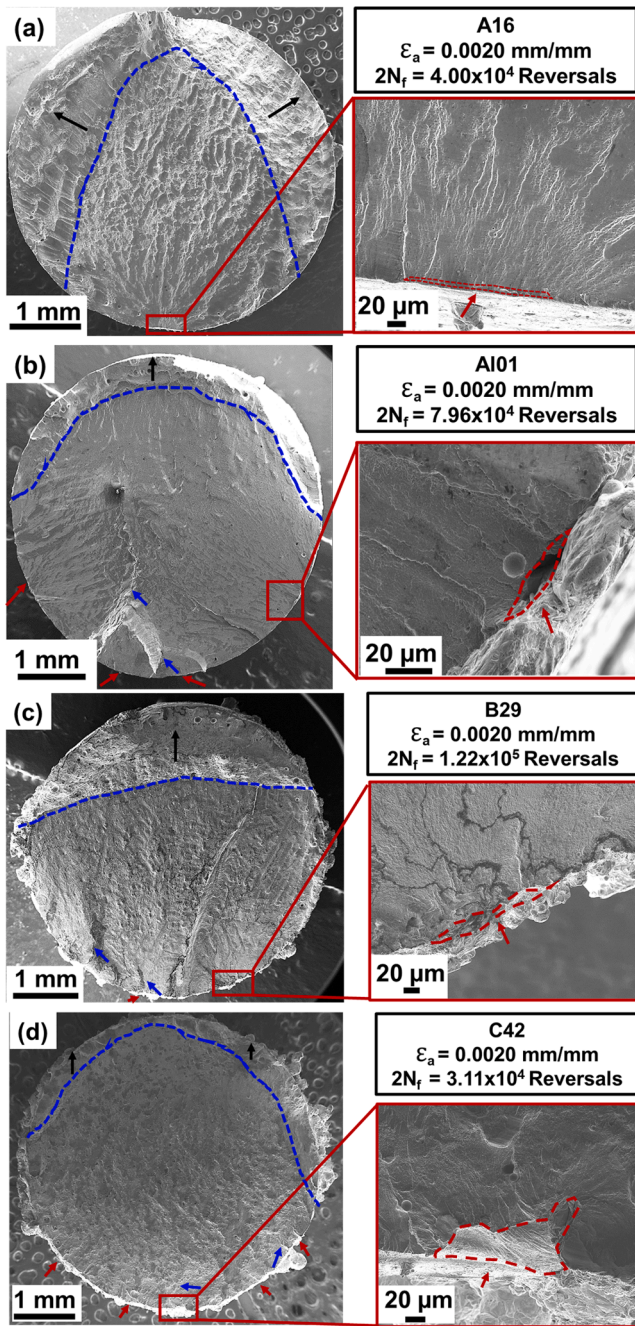
Fig. 13. Fracture surfaces of specimens tested in as-built surface condition at 0.0020 mm/mm strain amplitude: (a) LPW AlSi10Mg, (b) EOS AlSi10Mg, (c) Scalmalloy, and (d) QuesTek Al. The red, blue, and black arrows are indicating crack initiations, the coalescence of fatigue cracks after initial growth, and the final fracture area, respectively. (For interpretation of the references to colour in this figure legend, the reader is referred to the web version of this article.)

Fig. 14. (a) Strain-life and (b) stress-life fatigue data of LB-PBF Al specimens in machined surface condition.

The comparable fatigue lives of LPW and EOS AlSi10Mg in the MCF and LCF regimes (i.e., regimes where the crack propagation can be a major portion of the overall fatigue life) may be ascribed to two reasons; first, the higher ductility of LPW AlSi10Mg (see Fig. 6) as compared to the EOS counterpart, which can result in a higher crack propagation resistance [64]. The higher crack growth resistance not only increases the fatigue life, specifically in lower life regimes, but it also gives time to other defects to initiate cracks [65]. Second, the high strength Si networks present in the microstructure of EOS AlSi10Mg might have caused faster crack growth and further alleviated the fatigue resistance of this material. In the HCF regime, it can be seen in Fig. 14 and Table 6 that
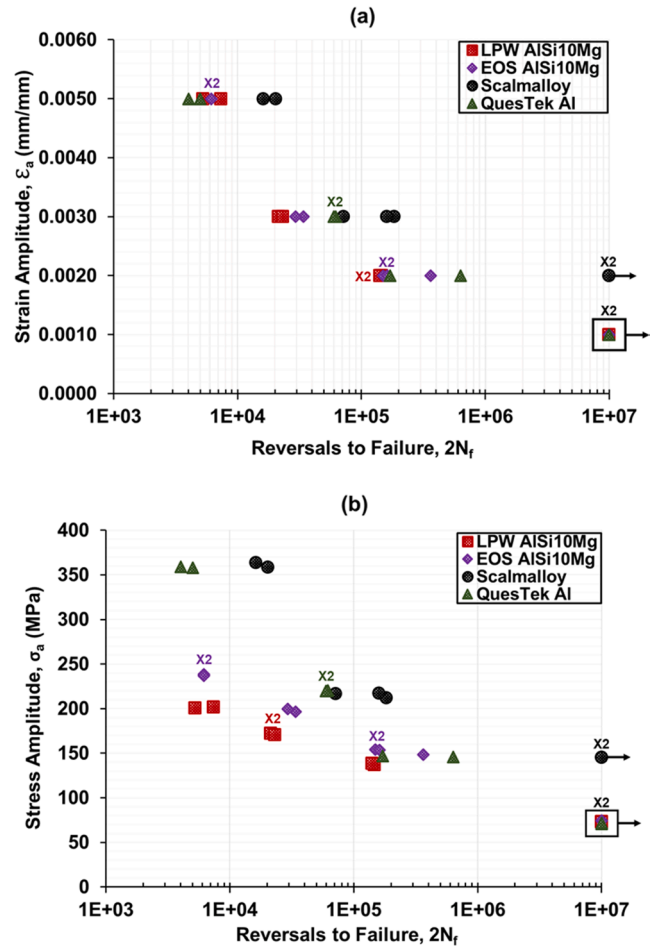
although the EOS AlSi10Mg specimens have somewhat larger defects as compared to the LPW AlSi10Mg counterparts, their fatigue lives are comparable. Knowing the fact that the most portion of fatigue life in HCF regime is typically spent in the crack nucleation stage [49], the high strength Si networks in EOS AlSi10Mg microstructure (see Fig. 10(b)), surrounding the volumetric defects, may have retarded the crack nucleation and resulted in comparable fatigue lives to those of the LPW counterparts (e.g., Al'37 vs. A'18 in Table 6).

From the fracture surface of the LB-PBF Scalmalloy specimen in Fig. 15(c), it can be seen that the crack initiated from an internal LoF defect forming a fisheye-like feature (specimen B'02 with 183,086 reversals to failure). Although this Scalmalloy specimen has a very large internal LoF defect ($\sqrt{area}$ = 157 μm), it has a longer fatigue life as compared to the other Al alloys tested at the same strain amplitude. This may be attributed to, first, its nano-size grain structure surrounding the volumetric defects, which can delay the crack initiation [66]. Secondly, Scalmalloy, with high strength and ductility, is expected to have a high fracture toughness [67], which may reduce the crack propagation rate [68].

For the LB-PBF QuesTek Al specimen (specimen C'02 with 61,778 reversals to failure) shown in Fig. 15(d), the crack initiated from a surface LoF defect with the $\sqrt{area}$ of 89 μm. Even though the crack initiated from a smaller defect in this QuesTek Al specimen, it has a shorter fatigue life as compared to the Scalmalloy counterpart in Fig. 15 (c). QuesTek Al is expected to have a lower crack initiation resistance due to its larger grain structure compared to the Scalmalloy. Furthermore, although the QuesTek Al has comparable strength to Scalmalloy, its lower ductility may result in a reduced fracture toughness;
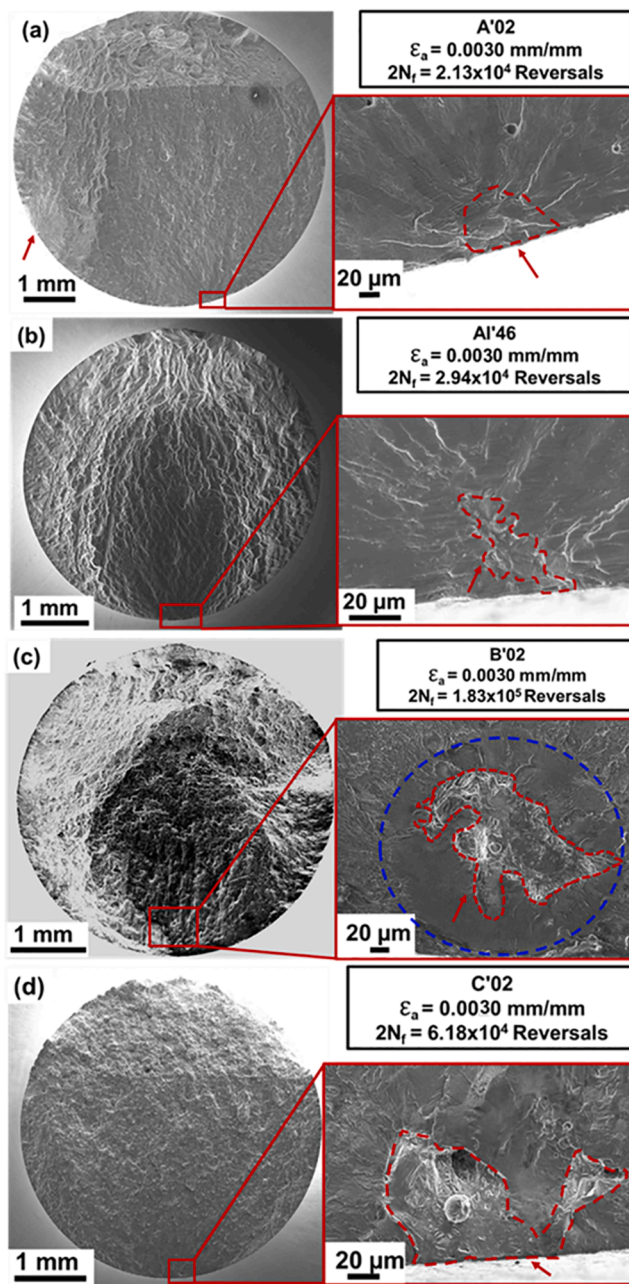
Fig. 15. Fracture surfaces of LB-PBF Al alloys tested in machined surface condition at 0.0030 mm/mm strain amplitude: (a) LPW AlSi10Mg, (b) EOS AlSi10Mg, (c) Scalmalloy, and (d) QuesTek Al. The red arrows indicate the crack initiation sites, and the blue curve shows the fisheye-like feature. (For interpretation of the references to colour in this figure legend, the reader is referred to the web version of this article.)

consequently, QuesTek Al is expected to have a lower crack propagation resistance as compared to Scalmalloy. Therefore, both the lower crack initiation resistance and higher crack propagation rate in QuesTek Al specimens may have contributed to the lower fatigue performance of QuesTek Al specimens as compared to the Scalmalloy counterparts.

On the other hand, the QuesTek Al machined specimens exhibit comparable fatigue performance to the AlSi10Mg counterparts despite the fact that they have larger defects than LPW and EOS AlSi10Mg specimens. This may be due to the finer grain structure of QuesTek Al specimens as compared to the LPW and EOS AlSi10Mg ones. The finer grain structure can result in higher crack initiation resistance in QuesTek Al specimens. However, one may consider that the larger defects in

QuesTek Al than the AlSi10Mg counterparts may have already deteriorated its fatigue performance. Indeed, considering the finer grain structure and the higher strength of QuesTek Al, it is postulated that this material can exhibit a better fatigue performance than AlSi10Mg if the process parameters are better optimized.

5. Conclusions

In this study, tensile and fatigue behaviors of four different LB-PBF Al alloys: LPW AlSi10Mg, EOS AlSi10Mg, Scalmalloy, and a new Al alloy developed by QuesTek Innovations LLC., were investigated. In addition, the effect of surface condition (as-built versus machined surface) on the fatigue properties of these alloys was studied. The mechanical behaviors observed were explained by characterizing the microstructure. It was found that the microstructure, including the grain size and precipitates, as well as the volumetric defects (i.e., pores, LoF), could play a significant role in the tensile and fatigue behavior of the LB-PBF Al alloys. The following conclusions could be drawn based on the obtained experimental results and analysis presented:

1. The microstructure of LB-PBF AlSi10Mg varied depending on the powder batch (LPW vs. EOS) and due to a slight difference in the stress relieving procedure. The LPW AlSi10Mg consisted of fine Si particles, while the EOS AlSi10Mg had an intercellular Si network structure.
2. Due to the presence of the high strength intercellular Si networks in the microstructure of the EOS AlSi10Mg, it had higher tensile strength and lower ductility as compared to the LPW AlSi10Mg.
3. The LB-PBF Scalmalloy consisted of nano-size equiaxed grains along with fine columnar grains. The grain refinement in the Scalmalloy was ascribed to the formation of the coherent nano-size $Al_3(Sc,Zr)$ precipitates during fabrication.
4. The LB-PBF Scalmalloy was found to have the highest tensile strength among all the alloys while also exhibiting a relatively high ductility. This behavior was attributed to the presence of nano-size precipitates and ultrafine/nano-size grain structure from the manufacturing process, as well as the formation of more nano-size precipitates after heat treatment.
5. The LB-PBF Scalmalloy exhibited considerably higher fatigue resistance as compared to the other alloys in both as-built and machined surface conditions, which makes it a better candidate for fatigue critical applications. The QuesTek Al had the lowest fatigue resistance in the as-built surface condition while possessed comparable fatigue resistance with that of LB-PBF AlSi10Mg specimens in machined surface condition. It should be mentioned that the surface process parameters were not optimized for Scalmalloy and QuesTek Al specimens.
6. Surface micro-notches were found to be the cause of fatigue crack initiations for the as-built surface specimens of all the LB-PBF Al alloys. For the machined surface condition, however, the cracks were initiated from the volumetric defects, either pores or LoF.
7. Machined LB-PBF Scalmalloy and QuesTek Al specimens, having fine grains surrounding the volumetric defects, were found to be more resistant to the fatigue crack initiation process compared to LPW and EOS AlSi10Mg. However, the lower ductility of QuesTek Al specimens has made them more sensitive to the presence of defects, resulting in lower fatigue lives compared to the Scalmalloy specimens and comparable fatigue performance to LPW and EOS AlSi10Mg specimens.

Declaration of Competing Interest

The authors declare that they have no known competing financial interests or personal relationships that could have appeared to influence the work reported in this paper.

Acknowledgments

Partial supports from the U.S. Naval Air Systems Command (NAV-AIR) and EOS North America Inc. are acknowledged.

References

[1] Rendigs KH. Aluminium Structures Used in Aerospace - Status and Prospects-. Mater Sci Forum 1997;242:11–24.

[2] Zhang J, Song B, Wei Q, Bourell D, Shi Y. A review of selective laser melting of aluminum alloys: Processing, microstructure, property and developing trends. J Mater Sci Technol 2019;35:270–84.

[3] Cui CX, Shen YT, Meng FB, Kang SB. Review on fabrication methods of in situ metal matrix composites. J Mater Sci Technol 2000;16:619–26.

[4] Branco R, Costa J, Berto F, Razavi S, Ferreira J, Capela C, et al. Low-cycle fatigue behaviour of AISI 18Ni300 maraging steel produced by selective laser melting. Metals (Basel) 2018;8:32.

[5] Bremen S, Meiners W, Diatlov A. Selective laser melting. Laser Tech J 2012;9:33–8.

[6] Yadollahi A, Shamsaei N. Additive manufacturing of fatigue resistant materials: Challenges and opportunities. Int J Fatigue 2017;98:14–31.

[7] Gockel J, Sheridan L, Koerper B, Whip B. The influence of additive manufacturing processing parameters on surface roughness and fatigue life. Int J Fatigue 2019; 124:380–8.

[8] Torries B, Sterling AJ, Shamsaei N, Thompson SM, Daniewicz SR. Utilization of a microstructure sensitive fatigue model for additively manufactured Ti-6Al-4V. Rapid Prototyp J 2016;22:817–25.

[9] Romano S, Brückner-Foit A, Brandão A, Gumpinger J, Ghidini T, Beretta S. Fatigue properties of AlSi10Mg obtained by additive manufacturing: Defect-based modelling and prediction of fatigue strength. Eng Fract Mech 2018;187:165–89.

[10] Brandl E, Heckenberger U, Holzinger V, Buchbinder D. Additive manufactured AlSi10Mg samples using Selective Laser Melting (SLM): Microstructure, high cycle fatigue, and fracture behavior. Mater Des 2012;34:159–69.

[11] Properties of Pure Aluminum. Alum Sci Technol, ASM International, 2018:31–43.

[12] MacLeod HA, Macleod HA. Thin-film optical filters. CRC Press; 2010.

[13] Fulcher BA, Leigh DK, Watt TJ. Comparison of AlSi10Mg and Al 6061 Processed Through DMLS. In: Proc. 25th Solid Free. Fabr. Symp.; 2014. p. 404–19.

[14] Zhang W, Hu Y, Ma X, Qian G, Zhang J, Yang Z, et al. Very-high-cycle fatigue behavior of AlSi10Mg manufactured by selected laser melting: Crystal plasticity modeling. Int J Fatigue 2021;145:106109.

[15] Jian ZM, Qian GA, Paolino DS, Tridello A, Berto F, Hong YS. Crack initiation behavior and fatigue performance up to very-high-cycle regime of AlSi10Mg fabricated by selective laser melting with two powder sizes. Int J Fatigue 2021;143:106013.

[16] Qian G, Jian Z, Qian Y, Pan X, Ma X, Hong Y. Very-high-cycle fatigue behavior of AlSi10Mg manufactured by selective laser melting: Effect of build orientation and mean stress. Int J Fatigue 2020;138:105696.

[17] Brandão AD, Gumpinger J, Gschweitl M, Seyfert C, Hofbauer P, Ghidini T. Fatigue properties of additively manufactured AlSi10Mg – surface treatment effect. Procedia Struct Integr 2017;7:58–66.

[18] Domfang Ngnekou JN, Nadot Y, Henaff G, Nicolai J, Kan WH, Cairney JM, et al. Fatigue properties of AlSi10Mg produced by Additive Layer Manufacturing. Int J Fatigue 2019;119:160–72.

[19] Thijs L, Kempen K, Kruth J-P, Van Humbeeck J. Fine-structured aluminium products with controllable texture by selective laser melting of pre-alloyed AlSi10Mg powder. Acta Mater 2013;61:1809–19.

[20] Tang M, Pistorius PC. Oxides, porosity and fatigue performance of AlSi10Mg parts produced by selective laser melting. Int J Fatigue 2017;94:192–201.

[21] Mann V, Krokhin A, Alabin A, Zmanovskiy S, Konkevich V, Redkin I. Evolution of aluminum alloys structure at production phases of 3D products by methods of additive technologies. In: Miner. Met. Mater. Ser.; 2017. p. 49–59.

[22] APWORKS AIRBUS GmbH. Scalmalloy-state of the art high-strength alloy.

[23] DebRoy T, Wei HL, Zuback JS, Mukherjee T, Elmer JW, Milewski JO, et al. Additive manufacturing of metallic components – Process, structure and properties. Prog Mater Sci 2018;92:112–224.

[24] Zhou L, Pan H, Hyer H, Park S, Bai Y, McWilliams B, et al. Microstructure and tensile property of a novel AlZnMgScZr alloy additively manufactured by gas atomization and laser powder bed fusion. Scr Mater 2019;158:24–8.

[25] Spierings AB, Dawson K, Kern K, Palm F, Wegener K. SLM-processed Sc- and Zr-modified Al-Mg alloy: Mechanical properties and microstructural effects of heat treatment. Mater Sci Eng A 2017;701:264–73.

[26] Spierings AB, Dawson K, Dumitraschkewitz P, Pogatscher S, Wegener K. Microstructure characterization of SLM-processed Al-Mg-Sc-Zr alloy in the heat treated and HIPed condition. Addit Manuf 2018;20:173–81.

[27] Li R, Chen H, Chen C, Zhu H, Wang M, Yuan T, et al. Selective laser melting of gas atomized Al–3.02Mg–0.2Sc–0.1Zr alloy powder: microstructure and mechanical properties. Adv Eng Mater 2019;21:1800650.

[28] Ahmad Z. The properties and application of scandium-reinforced aluminum. JOM 2003;55:35–9.

[29] Awd M, Tenkamp J, Hirtler M, Siddique S, Bambach M, Walther F. Comparison of microstructure and mechanical properties of scalmalloy® produced by selective laser melting and laser metal deposition. Materials (Basel) 2017;11:17.

[30] Begoc S, Montredon F, Pommatau G, Leger G, Gas M. Additive manufacturing of Scalmalloy ® satellite parts. 8Th Eur. Conf. Aeronaut. Sp. Sci.. 2019.

[31] America Makes AMSC. Standardization Roadmap for Additive Manufacturing - Version 2.0, America Makes ANSI Addit. Manuf Stand Collab 2018;2:1–203.

[32] Metal Powder Production for Additive Manufacturing | Carpenter Additive.

[33] Jia Q, Rometsch P, Kürnsteiner P, Chao Q, Huang A, Weyland M, et al. Selective laser melting of a high strength Al Mn Sc alloy: Alloy design and strengthening mechanisms. Acta Mater 2019;171:108–18.

[34] ASTM E606/E606M. Standard Test Method for Strain-Controlled Fatigue Testing, ASTM Stand, 2012.

[35] ASTM E8/E8M-13a. Standard Test Methods for Tension Testing of Metallic Materials, ASTM Stand, 2013.

[36] Bagherifard S, Beretta N, Monti S, Riccio M, Bandini M, Guagliano M. On the fatigue strength enhancement of additive manufactured AlSi10Mg parts by mechanical and thermal post-processing. Mater Des 2018;145:28–41.

[37] Maamoun AH, Elbestawi M, Dosbaeva GK, Veldhuis SC. Thermal post-processing of AlSi10Mg parts produced by Selective Laser Melting using recycled powder. Addit Manuf 2018;21:234–47.

[38] Fousová M, Dvorský D, Michalcová A, Vojtěch D. Changes in the microstructure and mechanical properties of additively manufactured AlSi10Mg alloy after exposure to elevated temperatures. Mater Charact 2018;137:119–26.

[39] Shi Y, Yang K, Kairy SK, Palm F, Wu X, Rometsch PA. Effect of platform temperature on the porosity, microstructure and mechanical properties of an Al–Mg–Sc–Zr alloy fabricated by selective laser melting. Mater Sci Eng A 2018;732:41–52.

[40] ASTM E2627. Standard Practice for Determining Average Grain Size Using Electron Backscatter Diffraction (EBSD) in Fully Recrystallized Polycrystalline Materials, ASTM Stand, 2019.

[41] Griffiths S, Rossell MD, Croteau J, Vo NQ, Dunand DC, Leinenbach C. Effect of laser rescanning on the grain microstructure of a selective laser melted Al-Mg-Zr alloy. Mater Charact 2018;143:34–42.

[42] ISO 4287: 1997 (en). Geometrical product specifications (GPS) -Surface texture: Profile method — Terms, definitions and surface texture parameters, Int. Stand. ISO, 2007.

[43] Liu Z, Cheng N, Zheng Q, Wu J, Han Q, Huang Z, et al. Processing and tensile properties of A356 composites containing in situ small-sized Al3Ti particulates. Mater Sci Eng A 2018;710:392–9.

[44] Kimura T, Nakamoto T. Microstructures and mechanical properties of A356 (AlSi7Mg0.3) aluminum alloy fabricated by selective laser melting. Mater Des 2016;89:1294–301.

[45] ASM International Handbook Committee. ASM Handbook Vol. 2: Properties and selection–nonferrous alloys and special-purpose materials, 2001.

[46] Uddin SZ, Murr LE, Terrazas CA, Morton P, Roberson DA, Wicker RB. Processing and characterization of crack-free aluminum 6061 using high-temperature heating in laser powder bed fusion additive manufacturing. Addit Manuf 2018;22:405–15.

[47] Koutny D, Skulina D, Pantělejev L, Paloušek D, Lenczowski B, Palm F, et al. Processing of Al-Sc aluminum alloy using SLM technology. Procedia CIRP 2018:44–8.

[48] Azadi M, Zolfaghari M, Rezanezhad S, Azadi M. Effects of SiO2 nano-particles on tribological and mechanical properties of aluminum matrix composites by different dispersion methods. Appl Phys A 2018;124:377.

[49] Stephens RRI, Fatemi A, Stephens RRI, Fuchs HO. Metal Fatigue in Engineering. 2nd ed., 2000.

[50] Nezhadfar PD, Shrestha R, Phan N, Shamsaei N. Fatigue behavior of additively manufactured 17–4 PH stainless steel: Synergistic effects of surface roughness and heat treatment. Int J Fatigue 2019;124:188–204.

[51] Dieter GE. Mechanical metallurgy. 3rd ed. Boston, MA, MA: McGraw-Hill; 1986.

[52] Rometsch P, Jia Q, Yang KV, Wu X. Aluminum alloys for selective laser melting – towards improved performance. Addit Manuf Aerosp Ind 2019:301–25.

[53] Li W, Li S, Liu J, Zhang A, Zhou Y, Wei Q, et al. Effect of heat treatment on AlSi10Mg alloy fabricated by selective laser melting: Microstructure evolution, mechanical properties and fracture mechanism. Mater Sci Eng A 2016;663:116–25.

[54] Wang YM, Voisin T, McKeown JT, Ye J, Calta NP, Li Z, et al. Additively manufactured hierarchical stainless steels with high strength and ductility. Nat Mater 2018;17:63–71.

[55] Beretta S, Gargourimotlagh M, Foletti S, du Plessis A, Riccio M. Fatigue strength assessment of "as built" AlSi10Mg manufactured by SLM with different build orientations. Int J Fatigue 2020;139:105737.

[56] Wang Z, Wu W, Qian G, Sun L, Li X, Correia JAFO. In-situ SEM investigation on fatigue behaviors of additive manufactured Al-Si10-Mg alloy at elevated temperature. Eng Fract Mech 2019;214:149–63.

[57] Hamidi Nasab M, Romano S, Gastaldi D, Beretta S, Vedani M. Combined effect of surface anomalies and volumetric defects on fatigue assessment of AlSi7Mg fabricated via laser powder bed fusion. Addit Manuf 2020;34:100918.

[58] Romano S, Nezhadfar PD, Shamsaei N, Seifi M, Beretta S. High cycle fatigue behavior and life prediction for additively manufactured 17–4 PH stainless steel: Effect of sub-surface porosity and surface roughness. Theor Appl Fract Mech 2020;106:102477.

[59] Sheridan L, Scott-Emuakpor OE, George T, Gockel JE. Relating porosity to fatigue failure in additively manufactured alloy 718. Mater Sci Eng A 2018.

[60] Brandão AD, Gumpinger J, Gschweitl M, Seyfert C, Hofbauer P, Ghidini T. Fatigue properties of additively manufactured AlSi10Mg-surface treatment effect. Procedia Struct Integr 2017.

[61] Muhammad M, Frye P, Simsiriwong J, Shao S, Shamsaei N. An investigation into the effects of cyclic strain rate on the high cycle and very high cycle fatigue behaviors of wrought and additively manufactured Inconel 718. Int J Fatigue 2021; 144:106038.

[62] Nezhadfar PD, Johnson AS, Shamsaei N. Fatigue behavior and microstructural evolution of additively manufactured Inconel 718 under cyclic loading at elevated temperature. Int J Fatigue 2020;136:105598.

[63] Pegues JW, Roach MD, Shamsaei N. Additive manufacturing of fatigue resistant austenitic stainless steels by understanding process-structure–property relationships. Mater Res Lett 2020;8:8–15.

[64] Nezhadfar PD, Anderson-Wedge K, Daniewicz SR, Phan N, Shao S, Shamsaei N. Improved high cycle fatigue performance of additively manufactured 17–4 PH stainless steel via in-process refining micro-/defect-structure. Addit Manuf 2020; 36:101604.

[65] Shamsaei N, Fatemi A. Small fatigue crack growth under multiaxial stresses. Int J Fatigue 2014;58:126–35.

[66] Taira S, Tanaka K, Hoshina M. Grain size effect on crack nucleation and growth in long-life fatigue of low-carbon steel. In: Fatigue Mech. ASTM International; 1979. p. 135–73.

[67] Hahn GT, Rosenfield AR. Sources of fracture toughness: The relationship between KIC and the ordinary tensile properties of metals. Appl Relat Phenom Titan Alloy 1967.

[68] Sawaki Y, Tada S, Hashimoto S, Kawasaki T. Fatigue fracture toughness and crack propagation rate. Int J Fract 1987;35:125–37.